Universiteit
Leiden
The Netherlands

The hunt for red dwarf binaries and hot planets in the WFCAM transit survey

Nefs, S.V.

Citation
Nefs, S. V. (2013, March 27). *The hunt for red dwarf binaries and hot planets in the WFCAM transit survey*. Retrieved from https://hdl.handle.net/1887/20669

Version:	Not Applicable (or Unknown)
License:	Leiden University Non-exclusive license
Downloaded from:	https://hdl.handle.net/1887/20669

Note: To cite this publication please use the final published version (if applicable).

Cover Page

Universiteit Leiden

The handle http://hdl.handle.net/1887/20669 holds various files of this Leiden University dissertation.

Author: Nefs, Bas
Title: The hunt for red dwarf binaries and hot planets in the WFCAM transit survey
Issue Date: 2013-03-27

Chapter 3

Discovery and characterisation of detached M-dwarf eclipsing binaries in the WFCAM Transit Survey

We report the discovery of 16 detached M-dwarf eclipsing binaries with $J < 16$ mag and provide a detailed characterisation of three of them, using high-precision infrared light curves from the WFCAM Transit Survey (WTS). Such systems provide the most accurate and model-independent method for measuring the fundamental parameters of these poorly understood yet numerous stars, which currently lack sufficient observations to precisely calibrate stellar evolution models. We fully solve for the masses and radii of three of the systems, finding orbital periods in the range $1.5 < P < 4.9$ days, with masses spanning $0.35-0.50\mathrm{M}_{\odot}$ and radii between $0.38-0.50\mathrm{R}_{\odot}$, with uncertainties of $\sim 3.5-6.4\%$ in mass and $\sim 2.7-5.5\%$ in radius. Close-companions in short-period binaries are expected to be tidally-locked into fast rotational velocities, resulting in high levels of magnetic activity. This is predicted to inflate their radii by inhibiting convective flow and increasing star spot coverage. The radii of the WTS systems are inflated above model predictions by $\sim 3-12\%$, in agreement with the observed trend, despite an expected lower systematic contribution from star spots signals at infrared wavelengths. We searched for correlation between the orbital period and radius inflation by combining our results with all existing M-dwarf radius measurements of comparable precision, but we found no statistically significant evidence for a decrease in radius inflation for longer period, less active systems. Radius inflation continues to exists in non-synchronised systems indicating that the problem remains even for very low activity M-dwarfs. Resolving this issue is vital not only for understanding the most populous stars in the Universe, but also for characterising their planetary companions, which hold the best prospects for finding Earth-like planets in the traditional habitable zone.

J.L.B. Birkby, **S.V. Nefs**, S.T. Hodgkin, G. Kovács, B. Sipőcz
, D.J. Pinfield, I.A.G. Snellen, D. Mislis, F. Murgas, N. Lodieu
E. de Mooij, N. Goulding, P. Cruz, H. Stoev, M. Cappetta
E. Palle, D. Barrado, R. Saglia, E. Martin, Y. Pavlenko
MNRAS 426, B1507 (2012)

3.1 Introduction

M-dwarfs ($M_\star \lesssim 0.6\mathrm{M}_\odot$) constitute more than seventy per cent of the Galactic stellar population (Henry et al. 1997) and consequently, they influence a wide-range of astrophysical phenomena, from the total baryonic content of the universe, to the shape of the stellar initial mass function. Furthermore, they are fast becoming a key player in the hunt for Earth-like planets (e.g. Nutzman & Charbonneau 2008; Koppenhoefer et al. 2009; Law et al. 2011). The lower masses and smaller radii of M-dwarfs mean that an Earth-like companion causes a deeper transit and induces a greater reflex motion in its host than it would do to a solar analogue, making it comparatively easier to detect Earths in the traditional habitable zones of cool stars. The inferred properties of exoplanet companions, such as their density, atmospheric structure and composition, currently depend on a precise knowledge of the fundamental properties of the host star, such as its mass, radius, luminosity and effective temperature at a given age. Yet, to date, no theoretical model of low-mass stellar evolution can accurately reproduce all of the observed properties of M-dwarfs (Hillenbrand & White 2004; López-Morales & Ribas 2005), which leaves their planetary companions open to significant mischaracterisation. Indeed, the characterisation of the atmosphere of the super-Earth around the M-dwarf GJ 1214 seems to depend on the spot coverage of the host star (de Mooij et al. 2012).

Detached, double-lined, M-dwarf eclipsing binaries (MEBs) provide the most accurate and precise, model-independent means of measuring the fundamental properties of low-mass stars (Andersen 1991), and the coevality of the component stars, coupled with the assumption that they have the same metallicity due to their shared natal environment, places stringent observational constraints on stellar evolution models. In the best cases, the uncertainties on the masses and radii measured using MEBs can be just 0.5% (Morales et al. 2009; Kraus et al. 2011). However, since M-dwarfs are intrinsically faint, only a small number of MEBs have been characterised so far with suitable accuracy to calibrate low-mass stellar evolution models, and there are even fewer measurements below $\sim 0.35\mathrm{M}_\odot$, where stellar atmospheres are thought to transport energy purely by convection (Chabrier & Baraffe 1997).

More worryingly, existing observations show significant discrepancies with stellar models. The measured radii of M-dwarfs are inflated by $5-10\%$ compared to model estimates and their effective temperatures appear too cool by $3-5\%$ (see e.g. Torres & Ribas 2002; López-Morales & Ribas 2005; Ribas 2006; Morales et al. 2010; Torres et al. 2010; Kraus et al. 2011). This anomaly has been known for some time but remains enigmatic. Bizarrely, the two discrepancies compensate each other in the mass-luminosity plane such that current stellar models can accurately reproduce the observed mass-luminosity relationship for M-dwarfs. Two different physical mechanisms have been suggested as the cause of this apparent radius inflation: i) metallicity (Berger et al. 2006; López-Morales 2007) and ii) magnetic activity (Mullan & MacDonald 2001; Ribas 2006; Torres et al. 2006; Chabrier et al. 2007).

Berger et al. (2006) and López-Morales (2007) used interferometrically-measured radii of single, low-mass stars to look for correlation between inflation and metallicity. Both studies found evidence that inactive, single stars with inflated radii corresponded to stars with higher metallicity, but this did not hold true for active, fast-rotating single stars and further studies could not confirm the result (Demory et al. 2009). While metallicity may play a role in the scatter of effective temperatures for a given mass (the effective temperature depends on the bolometric luminosity which is a function of metallicity), it seems unlikely that it is the main

culprit of radius inflation.

The magnetic activity hypothesis is steered by the fact that the large majority of well-characterised MEBs are in short (< 2 day) orbits. Such short period systems found in the field (i.e. old systems) are expected to be tidally-synchronised with circularised orbits (Zahn 1977). The effect of tidal-locking is to increase magnetic activity and is a notion that is supported by observations of synchronous, rapid rotation rates in MEBs, a majority of circular orbits for MEBs, plus X-ray emission and Hα emission from at least one of the components. It is hypothesised that increased magnetic activity affects the radius of the star in two ways. Firstly, it can inhibit the convective flow, thus the star must inflate and cool to maintain hydrostatic equilibrium. Chabrier et al. (2007) modelled this as a change in the convective mixing length, finding that a reduced mixing length could account for the inflated radii of stars in the partially-radiative mass regime, but it had negligible effect on the predicted radii of stars in the fully-convective regime. However, Jackson et al. (2009) showed that the radii of young, single, active, fully-convective stars in the open cluster NGC 2516 could be inflated by up to 50%, based on radii derived using photometrically-measured rotation rates and spectroscopically-measured projected rotational velocities. This therefore suggests that inhibition of convective flow is not the only factor responsible for the radius anomaly.

The second consequence of increased magnetic activity is a higher production of photospheric spots which has a two-fold effect: i) a loss of radiative efficiency at the surface, causing the star to inflate and ii) a systematic error in light curve solutions due to a loss of circular symmetry caused by a polar distribution of spots. Morales et al. (2010) showed that these two effects could account for $\sim 3\%$ and $0-6\%$ of the radius inflation, respectively, with any any remaining excess $(0-4\%)$ produced by inhibition of convective efficiency. This however is only under certain generalisations, such as a 30% spot coverage fraction and a concentration of the spot distribution at the pole. One would perhaps expect the systematic error induced by star spots to be wavelength dependant, such that radius measurements obtained at longer wavelength would be closer to model predictions.

Kraus et al. (2011) searched for correlation between the radius anomaly and the orbital periods of MEBs, to see if the data and the models converged at longer periods (~ 3 days) where the stellar activity is less aggravated by fast rotation speeds. They found tentative evidence to suggest that this is the case but it is currently confined to the realm of small statistics. Not long after their study, the MEarth project uncovered a 41-day, non-synchronised, non-circularised, inactive MEB with radius measurements still inflated on average by $\sim 4\%$, despite a detailed attempt to account for spot-induced systematics (Irwin et al. 2011). They suggest that either a much larger spot coverage than the 30% they assumed is required to explain the inflation, or perhaps that the equation of state for low-mass stars, despite substantial progress (see review by Chabrier et al. 2005), is still inadequate.

Clearly, a large sample of MEBs with a wide-range of orbital periods is key to defining the magnetic activity effect and understanding any further underlying physical issues for modelling the evolution of low-mass single stars. This in turn will remove many uncertainties in the properties of exoplanets with M-dwarf host stars. With that in mind, this paper presents the discovery of many new MEBs to emerge from the WFCAM Transit Survey, including a full characterisation to reasonable accuracy for three of the systems using 4-m class telescopes, despite their relatively faint magnitudes ($i = 16.7-17.6$).

In Section 3.2, we describe the WFCAM Transit Survey (WTS) and its observing strat-

egy, and Section 3.3 provides additional details of the photometric and spectroscopic data we used to fully characterise three of the MEBs. In Section 3.4, we outline how we identified the MEBs amongst the large catalogue of light curves in the WTS. Sections 3.5-3.7 present our analysis of all the available follow-up data used to characterise three of the MEBs including their system effective temperatures, metallicities, Hα emission and surface gravities, via analysis of low-resolution spectroscopy, their size-ratio and orbital elements using multi-colour light curves, and their mass ratios using radial velocities obtained with intermediate-resolution spectra. These results are combined in Section 3.8 to determine individual masses, radii, effective temperatures. We also calculate their space velocities and assess their membership to the Galactic thick and thin disks. Lastly, in Section 3.9, we discuss our results in the context of low-mass stellar evolution models and a mass-radius-period relationship, as suggested by Kraus et al. (2011).

3.2 The WFCAM Transit Survey

We identified our new MEBs using observations from the WFCAM Transit Survey (WTS) (Birkby et al. 2011). The WTS in an on-going photometric monitoring campaign that operates on the 3.8m United Kingdom Infrared Telescope (UKIRT) at Mauna Kea, Hawaii. Its primary and complementary science goals are: i) to provide a stringent observational constraint on planet formation theories through a statistically meaningful measure of the occurrence rate of hot Jupiters around low-mass stars (Kovacs et al. 2012; submitted) and ii) to detect a large sample of eclipsing binaries stars with low-mass primaries and characterise them to high enough accuracy such that we strongly constrain the stellar evolution models describing the planet-hosting M-dwarfs found in the survey. The WTS contains $\sim 6,000$ early to mid M-dwarfs with $J \leq 16$ mag, covering four regions of the sky which span a total of 6 square degrees.

We combine the large aperture of UKIRT with the Wide-Field Camera (WFCAM) infrared imaging array to observe in the J-band (1.25μm), near the peak of the spectral energy distribution (SED) of a cool star. Our observing strategy takes advantage of a unique opportunity offered by UKIRT, thanks to the highly efficient queue-scheduled operational mode of the telescope. Rather than requesting continuous monitoring, we noted there was room for a flexible proposal in the queue, which did not require the very best observing conditions, unlike most of the on-going UKIRT programmes that require photometric skies with seeing $< 1.3''$ (Lawrence et al. 2007). The WTS is therefore designed in such a way that there is always at least one target field visible and it can observe in mediocre seeing and thin cloud cover. We chose four target fields to give us year-round visibility, with each field passing within 15 degrees of zenith. To select the fields, we combined 2MASS photometry and the dust extinction maps of Schlegel et al. (1998) to find regions of sky that maximised the number of dwarf stars and maximised the ratio of dwarfs to giants (Cruz et al. 2003), while maintaining $E(B-V) < 0.1$. We stayed relatively close to the galactic plane to increase the number of early M-dwarfs, but restricted ourselves to $b > 5$ degrees to avoid the worst effects of overcrowding.

The survey began on August 05, 2007, and the eclipsing systems presented in this paper are all found in just one of the four WTS fields. The field is centred on RA = 19h, Dec = +36d, (hereafter, the 19h field), for which the WTS has its most extensive coverage, with 1145 data points as of June 16, 2011. Note that this field is very close to, but does not overlap with,

the Kepler field (Batalha et al. 2006), but it is promising that recent work showed the giant contamination in the Kepler field for magnitudes in a comparable range to our survey was low ($7 \pm 3\%$ M-giant fraction for $K_P > 14$), Mann et al. 2012.

3.3 Observations and Data Reduction

3.3.1 UKIRT/WFCAM *J*-band photometry

UKIRT and the WFCAM detector provide the survey with a large database of infrared light curves in which to search for transiting and eclipsing systems. The WFCAM detector consists of four 2048×2048 18μm pixel HgCdTe Rockwell Hawaii-II, non-buttable, infrared arrays that each cover $13.65' \times 13.65'$ and are separated by 94% of a chip width (Casali et al. 2007). Each WTS field covers 1.5 square degrees of sky, comprising of eight pointings of the WFCAM paw print, exposing for a 9-point jitter pattern with 10 second exposures at each position, and tiled to give uniform coverage across the field. It takes 15 minutes to observe an entire WTS field ($9 \times 10\text{s} \times 8+$overheads), resulting in a cadence of 4 data points per hour (corresponding to one UKIRT Minimum Schedulable Block). Unless there are persistently bad sky conditions at Mauna Kea, due to our relaxed observing constraints the WTS usually observes only at the beginning of the night, just after twilight in $> 1''$ seeing when the atmosphere is still cooling and settling.

The 2-D image processing of the WFCAM observations and the generation of light curves closely follows that of Irwin et al. (2007b) and is explained in detail in Kovacs et al. (2012;submitted). We refer the avid reader to these publications for an in-depth discussion of the reduction techniques but briefly describe it here. For image processing, we use the automatically reduced images from the Cambridge Astronomical Survey Unit pipeline[1], which is based on the INT wide-field survey pipeline (Irwin & Lewis 2001). This provides the 2-D instrumental signature removal for infrared arrays including the removal of the dark and reset anomaly, the flat-field correction using twilight flats, decurtaining and sky subtraction. We then perform astrometric calibration using 2MASS stars in the field-of-view, resulting in an astrometric accuracy of $\sim 20-50$ mas after correcting for field and differential distortion[2]. For photometric calibration, the detector magnitude zero-point is derived for each frame using measurements of stars in the 2MASS Point Source Catalogue that fall within the same frame (Hodgkin et al. 2009).

In order to generate a master catalogue of source positions for each field in the *J*-band filter, we stack 20 frames taken in the best conditions (i.e. seeing, sky brightness and transparency) and run our source detection software on the stacked image (Irwin 1985; Irwin & Lewis 2001). The resulting source positions are used to perform co-located, variable, 'soft-edged' (i.e. pro-rata flux division for boundary pixels) aperture photometry on all of the time-series images (see Irwin et al. 2007b).

For each of the four WFCAM detector chips, we model the flux residuals in each frame as a function of position using a 2-D quadratic polynomial, where the residuals are measured for each object as the difference between its magnitude on the frame in question and its median magnitude calculated across all frames. By subtracting the model fit, this frame-to-frame cor-

[1] http://casu.ast.cam.ac.uk/surveys−projects/wfcam/technical

[2] http://casu.ast.cam.ac.uk/surveys−projects/wfcam/technical/astrometry

rection can account for effects such as flat-fielding errors, or varying differential atmospheric extinction across each frame, which can be significant in wide-field imaging (see e.g. Irwin et al. 2007b).

Our source detection software flags any objects with overlapping isophotes. We used this information in conjunction with a morphological image classification flag also generated by the pipeline to identify non-stellar or blended objects. The plate scale of WFCAM ($0.4''$/pix) is significantly smaller than those of most small aperture, ground-based transit survey instruments, such as SuperWASP (Pollacco et al. 2006), HATNet (Bakos et al. 2004) and TrES (Dunham et al. 2004), and can have the advantage of reducing the numbers of blended targets, and therefore the numbers of transit mimics, despite observing fainter stars.

The last step in the light curve generation is to perform a correction for residual seeing-correlated effects caused by image blending that are not removed by the frame-to-frame correction. For each light curve, we model the deviations from its median flux as a function of the stellar image FWHM on the corresponding frame, using a quadratic polynomial that we then subtract. We note that this method addresses the symptoms, but not the cause, of the effects of blending.

Figure 3.1 shows the per data point photometric precision of the final light curves for the stellar sources in the 19hr field. The RMS is calculated as a robust estimator using as $1.48\times$MAD, i.e. the equivalent of the Gaussian RMS, where the MAD is the median of the absolute deviations (Hoaglin et al. 1983). The upturn between $J \sim 12-13$ mag marks the saturation limit, so for our brightest objects, we achieve a per data point precision of $\sim 3-5$ mmag. The blue solid line shows the median RMS in bins of 0.2 mag. The median RMS at $J = 16$ mag is $\sim 1\%$ (~ 10 mmag), with a scatter of $\sim 0.8-1.5\%$, and only 5% of sources have an RMS greater than 15 mmag at this magnitude. Hence, for the majority of sources with $J \leq 16$ mag, the precision is in theory suitable for detecting not only M-dwarf eclipsing binaries but also transits of mid-M stars by planets with radii $\sim 1R_{\oplus}$ (see Kovacs et al. (2012;submitted) for the WTS sensitivity to Jupiter- and Neptune-sized planets). The 16 new MEBs are shown on the plot by the red star symbols. Note that shorter period MEBs sit higher on the RMS diagram, but that genuine longer period MEBs still have RMS values close to the median, due to our robust estimator and the long observing baseline of the survey.

For the MEB light curves characterised in this paper, we perform an additional processing step, in which we use visual examination to clip several clear outlying data points at non-consecutive epochs.

The WTS *J*-band light curve data for the MEBs reported in this paper are given in Table 3.1. We have adopted a naming system that uniquely identifies each source handled by our data reduction process, and thus we refer to MEBs characterised in this paper as: 19b-2-01387, 19c-3-01405, and 19e-3-08413. The first number in the naming strategy gives the Right Ascension hour the target field. The following letter corresponds to one of the eight pointings that make up the whole WTS target field. The number between the hyphens denotes which of the four WFCAM chips the source is detected on and the final 5 digits constitute the source's unique sequence number in our master catalogue of WTS sources.

Some sources in the WTS fields are observed multiple times during a full field pointing sequence due to the slight overlap in the exposed areas in the tile pattern. 19c-3-01405 is one such target, receiving two measurements for every full field sequence. The median magnitude for 19c-3-01405 on each chip differs by 32 mmag. Hodgkin et al. (2009) claim a photometric

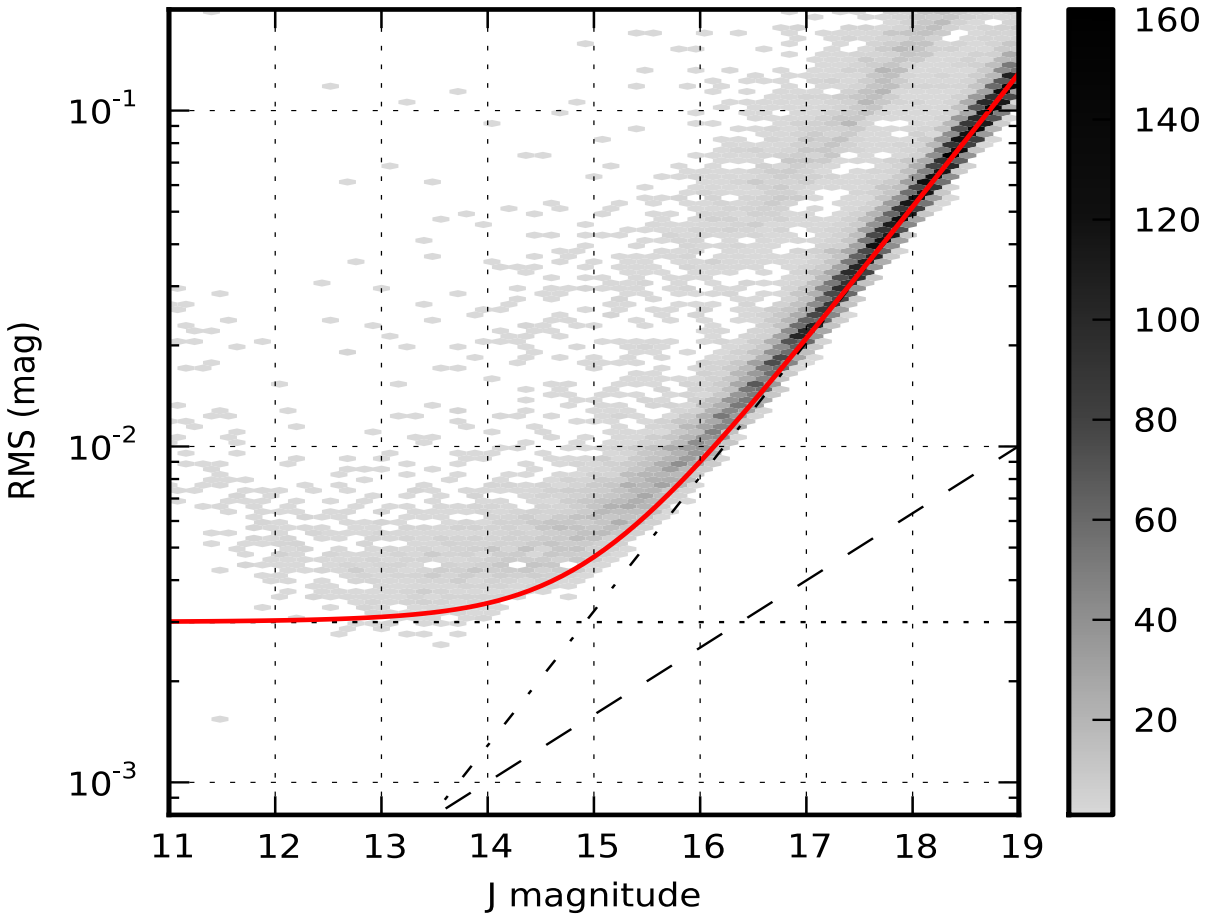

Figure 3.1 — The RMS scatter per data point of the WTS light curves as a function of WFCAM J magnitude, for sources in the 19hr field with stellar morphological classification. The RMS is a robust estimator calculated as 1.48 $\times$ the median of the absolute deviations. We achieve a per data point photometric precision of $3-5$ mmag for the brightest objects, with a median RMS of $\sim 1\%$ for $J = 16$ mag. Saturation occurs between $\sim 12-13$ mag as it varies across the field and with seeing. The dashed red horizontal line at 3 mmag marks the limit of our photometric precision. The blue solid curve shows the median RMS in bins of 0.2 mag. The red stars show the positions of the 16 WTS 19hr field MEBs. The shorter period MEBs sit higher in the plot. RMS values are given in Table 3.14

calibration error of 1.5% for WFCAM thus the median magnitudes have a $\sim 2\sigma$ calibration error. The photometric calibration uses 2MASS stars that fall on chip in question, so different calibration stars are used for different chips and pointing. We combined the light curves from both exposures to create a single light curve with $893 + 898 = 1791$ data points, after first subtracting the median flux from each light curve. The combined light curve has the same out-of-eclipse RMS, 8 mmag, as the two single light curves. The other two MEBs, 19b-2-01387 and 19e-3-08413, have 900 and 899 data points and an out-of-eclipse RMS of 5 mmag and 7 mmag, respectively.

We also obtained single, deep exposures of each WTS field in the WFCAM Z, Y, J, H and K filters (exposure times $180, 90, 90, 4 \times 90$ and 4×90 seconds, respectively). These are used

Name	HJD	$J_{\rm WTS}$ (mag)	$\sigma_{J_{\rm WTS}}$ (mag)	Δm_0^a (mag)	FWHM^b (pix)	x^c (pix)	y^c (pix)
19b-2-01387	2454317.808241	14.6210	0.0047	0.0001	2.17	321.98	211.07
19b-2-01387	2454317.820311	14.6168	0.0047	0.0002	2.37	321.74	210.88
...	...	...	...	...	...	...	...

Table 3.1 — The WTS J-band light curves of 19b-2-01387, 19c-3-01405 and 19e-3-08413. Magnitudes are given in the WFCAM system. Hodgkin et al. (2009) provide conversions for other systems. The errors, σ_J, are estimated using a standard noise model, including contributions from Poisson noise in the stellar counts, sky noise, readout noise and errors in the sky background estimation. [a] Correction to the frame magnitude zero point applied in the differential photometry procedure. More negative numbers indicate greater losses. See Irwin et al. (2007b). [b] Median FWHM of the stellar images on the frame. [c] x and y pixel coordinates the MEB systems on the image, derived using a standard intensity-weighted moments analysis. (This table is published in full in the online journal and is shown partially here for guidance regarding its form and content.)

in conjunction with g, r, i and z photometry from SDSS DR7 to create SEDs and derive first estimates of the effective temperatures for all sources in the field, as described in Section 3.4.1.

3.3.2 INT/WFC *i*-band follow-up photometry

Photometric follow-up observations to help test and refine our light curve models were obtained in the Sloan i-band using the Wide Field camera (WFC) on the 2.5m Isaac Newton Telescope (INT) at Roque de Los Muchachos, La Palma. We opted to use the INT's Sloan i filter rather than the RGO I-band filter as i) it has significantly less fringing and, ii) unlike the RGO filter, it has a sharp cut-off at ~ 8500 Å and therefore avoids strong, time-variable telluric water vapour absorption lines, which could induce systematics in our time-series photometry (Bailer-Jones & Lamm 2003). The observing run, between July 18 - August 01, 2010, was part of a wider WTS follow-up campaign to confirm planetary transit candidates and thus only a few windows were available to observe eclipses. Using the WFC in fast mode (readout time 28 sec. for 1×1 binning), we observed a full secondary eclipse of 19b-2-01387 and both a full primary and a full secondary eclipse of 19e-3-08413. The observations were centred around the expected times of primary and secondary eclipse, allowing at least 30 minutes of observation either side of ingress and egress to account for any uncertainty in our predicted eclipse times based on the modelling of the WTS light curves. In total, we observed 120 epochs for the secondary eclipse of 19b-2-01387 using 60s exposures, and 89 and 82 data points for the primary and secondary eclipse of 19e-3-08413, respectively, using 90s exposures.

We reduced the data using custom built IDL routines to perform the standard 2-D image processing (i.e. bias subtraction and flat-field division). Low-level fringing was removed by subtracting a scaled super sky-frame. To create the light curves, we performed variable aperture photometry using circular apertures with the IDL routine APER. The sky background was estimated using a 3σ-clipped median on a 30×30 pixel box, rejecting bad pixels. For each MEB, we selected sets of 15-20 bright, nearby, non-saturated, non-blended reference stars to create a master reference light curve. For each reference star, we selected the aperture with the smallest out-of-eclipse RMS. We removed the airmass dependence by fitting a second order polynomial

Name	HJD	$\Delta m_{i_{\rm INT}}$ (mag)	$\sigma_{m_{i_{\rm INT}}}$ (mag)
19b-2-01387	2455400.486275	-0.0044	-0.0034
19b-2-01387	2455400.487652	-0.0049	-0.0024
...	...	...	...

Table 3.2 — INT *i*-band follow-up light curves of 19b-2-01387 and 19e-3-08413. $\Delta m_{i_{\rm INT}}$ are the differential magnitudes with respect to the median of the out-of-eclipse measurements such that the out-of-eclipse magnitude is $m_{i_{\rm INT}} = 0$. The errors, σ_i, are the scaled Gaussian equivalents of the median absolute deviation of the target from the reference at each epoch i.e. $\sigma_i \sim 1.48 \times$ MAD. (This table is published in full in the online journal and is shown partially here for guidance regarding its form and content.)

to the out-of-eclipse data.

The INT *i*-band light curve data is presented in Table 3.2. The RMS of the out-of-eclipse data for the primary eclipse of 19b-2-01387 is 4.4 mmag while the out-of-eclipse RMS values for the primary and secondary eclipses of 19e-3-08413 are 5.7 mmag and 7.1 mmag, respectively.

3.3.3 IAC80/CAMELOT *g*-band follow-up photometry

We obtained a single primary eclipse of 19e-3-08413 in the Sloan *g*-band filter using the CAMELOT CCD imager on the 80cm IAC80 telescope at the Observatorio del Teide in Tenerife. The observations were obtained on the night of 08 August 2009, during a longer run to primarily follow-up WTS planet candidates. Exposure times were 60 seconds and were read out with 1×1 binning of the full detector, resulting in a cadence of 71 seconds, making a total of 191 observations for the night.

The time-series photometry was generated using the VAPHOT package[3] (Deeg & Doyle 2001). The bias and flat field images were processed using standard IRAF routines in order to calibrate the raw science images. The light curve was then generated using VAPHOT, which is a series of modified IRAF routines that performs aperture photometry; these routines find the optimum size aperture that maximize the signal-to-noise ratio for each star. The user can specify whether to use a variable aperture to account for a time-variable point-spread-function (e.g. due to changes in the seeing) or to fix it for all images. For this data set, we fixed the aperture and used an ensemble of 6 stars with a similar magnitude to the target to create a master reference light curve. Finally, a second order polynomial was fitted to the out-of-eclipse data the target light curve to remove a long-term systematic trend.

The *g*-band light curve is shown in the bottom left panel of Figure 3.6, and the data are given in Table 3.3. The out-of-eclipse RMS for the target is 26.9 mmag, which is higher than the follow-up with the INT, due to the smaller telescope diameter.

[3] http://www.iac.es/galeria/hdeeg/

HJD	$\Delta m_{g_{\rm IAC80}}$ (mag)	$\sigma_{m_{g_{\rm IAC80}}}$ (mag)
2455052.51020	-0.0417	0.0290
2455052.51113	-0.0091	0.0301
...	...	...

Table 3.3 — IAC80 g-band follow-up light curve of 19e-3-08413. $\Delta m_{g_{\rm IAC80}}$ are the differential magnitudes with respect to the median of the out-of-eclipse measurements such that the out-of-eclipse magnitude is $m_{g_{\rm IAC80}} = 0$. The errors, σ_g, are those computed by the IRAF.PHOT package. (This table is published in full in the online journal and is shown partially here for guidance regarding its form and content.)

Name	Epoch[a]	$t_{\rm int}$ (s)	Instr.	$\lambda_{\rm range}$ (Å)	R	SNR
19b-2-01387	394.71	300	ISIS	6000-9200	1000	27
19c-3-01405	426.53	900	ACAM	3300-9100	450	30
19e-3-08413	426.54	900	ACAM	3300-9100	450	30

Table 3.4 — Summary of low resolution spectroscopic observations at the William Herschel Telescope, La Palma. [a] JD-2455000.0.

3.3.4 WHT low-resolution spectroscopy

We carried out low-resolution spectroscopy during a wider follow-up campaign of the WTS MEB and planet candidates on several nights between July 16 and August 17, 2010, using the William Herschel Telescope (WHT) at Roque de Los Muchachos, La Palma. These spectra allow the identification of any giant contaminants via gravity sensitive spectral features, and provide estimates of the effective system temperatures, plus approximate metallicities and chromospheric activity indicators (see section 3.5).

We used the Intermediate dispersion Spectrograph and Imaging System (ISIS) and the Auxiliary-port Camera (ACAM) on the WHT to obtain our low-resolution spectra. In all instances we used a $1.0''$ slit. We did not use the dichroic during the ISIS observations because it can induce systematics and up to 10% efficiency losses in the red arm, which we wanted to avoid given the relative faintness of our targets. Wavelength and flux calibrations were performed using periodic observations of standard lamps and spectrophotometric standard stars throughout the nights. Table 3.4 summarises our low-resolution spectroscopic observations.

The reduction of the low-resolution spectra was performed with a combination of IRAF routines and custom IDL procedures. In IDL, the spectra were trimmed to encompass the length of the slit, bias-subtracted and median-filtered to remove cosmic rays. The ACAM spectra were also flat-fielded. We corrected the flat fields for dispersion effects using a pixel-integrated sensitivity function. The IRAF.APALL routine was used to identify the spectra, subtract the background and optimally sum the flux in apertures along the trace. For the ISIS spectrum, wavelength and flux calibration was performed with the CuNe+CuAr standard lamps and ING flux standard SP2032+248. For ACAM, arc frames were used to determine the wavelength solution along the slit using a fifth order spline function fit with an RMS ~ 0.2Å. For flux-

calibration, we obtained reference spectra of the ING flux standard SP2157+261.

3.3.5 WHT/ISIS intermediate-resolution spectroscopy

Modelling the individual radial velocities (RVs) of components in a binary system provides their mass ratio and a lower limit on their physical separation. Combining this information with an inclination angle determined by the light curve of an eclipsing system ultimately yields the true masses and radii of the stars in the binary. We measured the RVs of the components in our MEBs using spectra obtained with the intermediate-resolution, single-slit spectrograph ISIS mounted on the WHT. We used the red arm with the R1200R grating centred on 8500Å, giving a wavelength coverage of $\sim 8100-8900$Å. The slit width was chosen to match the approximate seeing at the time of observation giving an average spectral resolution $R \sim 9300$. The spectra were processed entirely with IRAF, using the CCDPROC packages for instrumental signature removal. We optimally extracted the spectra for each object on each night and performed wavelength and flux calibration using the semi-automatic KPNO.DOSLIT package. Wavelength calibration was achieved using CuNe arc lamp spectra taken after each set of exposures and flux calibration was achieved using observations of spectrophotometric standards.

Radial velocities via cross-correlation

The region $8700-8850$Å contains a number of relatively strong metallic lines present in M-dwarfs and is free of telluric absorption lines making it amenable for M-dwarf RV measurements (Irwin et al. 2009). We used the IRAF implementation of the standard 1-D cross-correlation technique, FXCOR, to extract the RV measurements for each MEB component using synthetic spectra from the MARCS[4] spectral database (Gustafsson et al. 2008) as templates. The templates had plane-parallel model geometry, a temperature range from 2800-5500K incremented in 200K steps, solar metallicity, surface gravity $\log(g) = 5.0$ and a 2 km/s microturbulence velocity, which are all consistent with low-mass dwarf stars. The best-matching template i.e. the one that maximised the cross-correlation strength of the primary component for each object, was used to obtain the final RVs of the system, although note that the temperature of the best-matching cross-correlation template is not a reliable estimate of the true effective temperature. The saturated near-infrared Ca II triplet lines at $8498, 8542$ and 8662Å were masked out during the cross-correlation. A summary of our observations and the extracted radial velocities are given in table 3.5.

3.4 Identification of M-dwarf Eclipsing Binaries

3.4.1 The M-dwarf sample

It is possible to select M-dwarfs in WTS fields using simple colour-colour plots such as those shown in Figure 3.2, which were compiled using our deep WFCAM photometry plus magnitudes from SDSS DR7, which has a fortuitous overlap with the 19hr field. Jones et al. (1994) showed that the $(i-K)$ colour is a reasonable estimator for the effective temperature, however

[4] http://marcs.astro.uu.se/

Name	HJD	Slit ($''$)	t_{int} (n×sec)	SNR	Phase	RV_1 (km/s)	RV_2 (km/s)
19b-2-01387	2455395.55200	1.2	2×1200	22.7	0.1422	-143.2	8.0
19b-2-01387	2455396.46471	0.7	3×600	6.22	0.7513	23.7	-158.0
19b-2-01387	2455407.52383	1.0	3×900	14.0	0.1314	-137.9	-4.2
19b-2-01387	2455407.62644	1.0	3×1200	8.0	0.1998	-155.3	25.1
19b-2-01387	2455408.38324	1.0	3×900	9.1	0.7049	14.5	-157.6
19b-2-01387	2455408.51689	1.0	3×1200	12.8	0.7941	15.1	-153.7
19b-2-01387	2455408.63070	1.0	3×1200	13.4	0.8700	-9.8	-139.2
19b-2-01387	2455409.38673	1.0	3×1200	14.3	0.3745	-128.4	-4.8
19c-3-01405	2455407.43073	1.0	$1200+630$	6.4	0.2244	-62.5	57.0
19c-3-01405	2455407.47937	1.0	3×1200	5.3	0.2343	-57.0	52.7
19c-3-01405	2455407.58012	1.0	3×1200	5.3	0.2547	-63.8	54.6
19c-3-01405	2455408.46929	1.0	3×1200	6.0	0.4347	-21.7	22.0
19c-3-01405	2455409.56881	1.0	3×1200	6.0	0.6573	47.3	-52.6
19c-3-01405	2455409.68190	0.8	3×1200	5.1	0.6802	42.5	-64.4
19c-3-01405	2455409.47707	0.8	3×1200	7.5	0.6387	46.4	-43.6
19e-3-08413	2455408.42993	1.0	3×1200	7.1	0.6640	108.0	-46.5
19e-3-08413	2455408.56307	1.0	3×1200	8.7	0.7435	113.1	-58.4
19e-3-08413	2455409.43629	1.0	3×1200	8.9	0.2654	-24.8	140.9
19e-3-08413	2455409.52287	0.8	3×1200	7.5	0.3171	-27.6	125.6
19e-3-08413	2455409.61343	0.8	3×1200	7.5	0.3712	-9.4	109.1

Table 3.5 — Summary of intermediate-resolution spectroscopic observations. All observations were centred on 8500Å.

the eclipsing nature of the systems we are interested in can cause irregularities in the colour indices, especially since the WFCAM photometry was taken at different epochs to each other and the SDSS photometry. For example, a system of two equal mass stars in total eclipse result is 0.75 mag fainter compared to its out-of-eclipse magnitude. We made a more robust sample of M-dwarfs by estimating the effective temperature of each source in the 19h field via SED fitting of all the available passbands i.e. SDSS g,r,i and z-band plus WFCAM Z,Y,J,H and K-band. By rejecting the most outlying magnitudes from the best SED fit, one becomes less susceptible to errors from in-eclipse observations. Note that the SDSS u-band magnitudes of our redder sources are affected by the known red leak in the u filter and are hence excluded from the SED fitting process.

To perform the SED fitting, we first put all the observed photometry to the Vega system (see Hewett et al. 2006 and Hodgkin et al. 2009 for conversions). Although the WFCAM photometry is calibrated to $1.5-2\%$ with respect to 2MASS (Hodgkin et al. 2009), the 2MASS photometry also carries its own systematic error, so we assumed an extra 3% systematic error added in quadrature to the photometric errors for each source to account for calibration errors between different surveys. We used a simple χ^2 fitting routine to compare the data to a set of solar metallicity model magnitudes at an age of 1 Gyr from the stellar evolution models of Baraffe et al. (1998). We linearly interpolated the model magnitudes onto a regular grid of 5 K intervals from $1739-6554$ K, to enable a more precise location of the χ^2 minimum. If the worst fitting

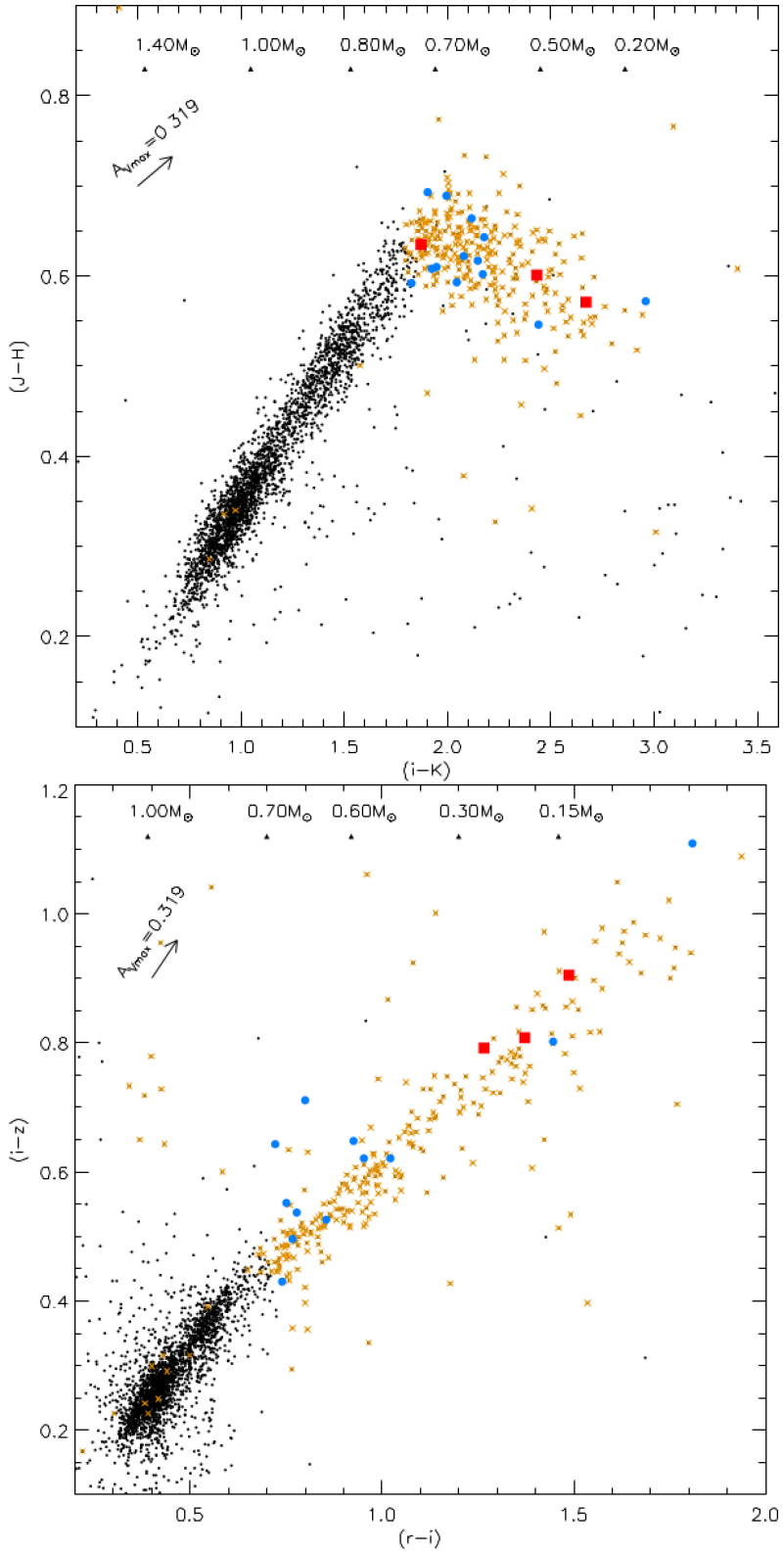

Figure 3.2 — Colour-colour plots of the sources in one of the WFCAM pointings for the 19hr field (black +), overlaid with the full 19hr field sample of detached MEB candidates (blue filled circles and red filled squares). The filled red squares mark the three MEB systems characterised in this paper. The orange crosses mark the M-dwarf candidate sources in the pointing (see Section 3.4.1). The triangles mark the masses for the given colour index, derived from the 1 Gyr solar metallicity isochrone of the Baraffe et al. (1998) low-mass stellar evolution models. The arrows mark the maximum reddening vector, assuming a distance of 1 kpc.

Parameter	19b-2-01387	19c-3-01405	19e-3-08413
α_{J2000}	19:34:15.5	19:36:40.7	19:32:43.2
δ_{J2000}	36:28:27.3	36:42:46.0	36:36:53.5
$\mu_\alpha cos\delta$ ($''$/yr)	0.023 ± 0.003	-0.002 ± 0.004	0.008 ± 0.004
μ_δ ($''$/yr)	0.032 ± 0.003	-0.001 ± 0.004	-0.007 ± 0.004
g	19.088 ± 0.010	20.342 ± 0.024	20.198 ± 0.020
r	17.697 ± 0.006	18.901 ± 0.012	18.640 ± 0.009
i	16.651 ± 0.004	17.634 ± 0.008	17.488 ± 0.005
z	16.026 ± 0.007	16.896 ± 0.012	16.847 ± 0.010
Z	15.593 ± 0.005	16.589 ± 0.007	16.156 ± 0.006
Y	15.188 ± 0.006	16.432 ± 0.011	15.832 ± 0.008
J	14.721 ± 0.004	15.706 ± 0.006	15.268 ± 0.005
H	14.086 ± 0.003	15.105 ± 0.006	14.697 ± 0.005
K	14.414 ± 0.006	14.836 ± 0.007	14.452 ± 0.006

Table 3.6 — A summary of photometric properties for the three MEBs, including our photometrically derived effective temperatures and spectral types. The proper motions $\mu_\alpha cos\delta$ and μ_δ are taken from the SDSS DR7 database. SDSS magnitudes g, r, i and z are in AB magnitudes, while the WFCAM Z, Y, J, H and K magnitudes are given in the Vega system. The errors on the photometry are the photon-counting errors and do not include the extra 3% systematic error we add in quadrature when performing the SED-fitting. Conversions of the WFCAM magnitudes to other systems can be found in Hodgkin et al. (2009). Note that the WFCAM K-band magnitude for 19b-2-01387 was obtained during an eclipse event and does not represent the total system magnitude.

data point in the best χ^2 fit was more than a 5σ outlier, we excluded that data point and re-ran the fitting procedure. This makes the process more robust to exposures taken in eclipse. The errors on the effective temperatures include the formal 1σ statistical errors from the χ^2 fit (which are likely to be under-estimated) plus an assumed ± 100 K systematic uncertainty. This error also takes into account the known missing opacity issue in the optical bandpasses in the Baraffe et al. (1998) models.

Our M-dwarf sample is conservative. It contains any source with an SED effective temperature ≤ 4209 K, magnitude $J \leq 16$ mag and a stellar class morphology flag (as determined by the data reduction pipeline). The maximum effective temperature corresponds to a radius of $0.66 R_\odot$ at the typical field star age of 1 Gyr, according to the stellar evolution models of Baraffe et al. (1998). We opted to restrict our MEB search to $J \leq 16$ mag because the prospects for ground-based radial velocity follow-up are bleak beyond $J = 16$ mag ($I \sim 18$ mag, Aigrain et al. 2007) if we wish to achieve accurate masses and radii that provide useful constraints on stellar evolution models. We found a total of $2,705$ M-dwarf sources in the 19hr field. Table 3.6 gives the single epoch, deep photometry from SDSS and WFCAM, plus the proper motions from the SDSS DR7 database (Munn et al. 2004, 2008) for the systems characterised in this paper. Their SED-derived system effective temperatures, $T_{eff,SED}$ are given in Table 3.7.

Interstellar reddening

The photometry for the 19hr field is not dereddened before performing the SED fitting. The faint magnitudes of our M-dwarf sources implies they are at non-negligible distances and that extinction along the line-of-sight may be significant. This means that our M-dwarf sample may contain hotter sources than we expect. At $J \leq 16$ mag, assuming no reddening, the WTS is distance-limited to ~ 1 kpc for the earliest M-dwarfs ($M_J = 6$ mag at 1 Gyr for M0V, $M_\star = 0.6\mathrm{M}_\odot$, using the models of Baraffe et al. 1998). We investigated the reddening effect in the direction of the 19hr field using a model for interstellar extinction presented by Drimmel et al. (2003). In this model, extinction does not have a simple linear dependency on distance but is instead a three-dimensional description of the Galaxy, consisting of a dust disk, spiral arms as mapped by HII regions, plus a local Orion-Cygnus arm segment, where dust parameters are constrained by COBE/DIRBE far infrared observations. Using this model, we calculate that $A_V = 0.319$ mag ($E(B-V) = 0.103$ mag) at 1 kpc in the direction of the 19hr field. We used the conversion factors in Table 6 of Schlegel et al. (1998) to calculate the absorption in the UKIRT and SDSS bandpasses, finding $A_g = 0.370$ mag, $A_K = 0.036$ mag, $E(r-i) = 0.065$, $E(i-z) = 0.059$ and $E(J-H) = 0.032$. The reddening affect along the line-of-sight to the field thus appears to be small. We show this maximum reddening vector as an arrow in Figure 3.2.

For the most interesting targets in the WTS (EBs or planet candidates), we obtain low-resolution spectra to further characterise the systems and check their dwarf-like nature (see Section 3.5). Effective temperatures based on spectral analysis suffer less from the effects of reddening effects because the analysis depends not only on the slope of the continuum but also the shape of specific molecular features, unlike the SED fitting. Therefore, the SED effective temperatures are only a first estimate and we will later adopt values derived by fitting model atmospheres to low-resolution spectra of our MEBs (see Section 3.5.4).

3.4.2 Eclipse detection

We made the initial detection of our MEBs during an automated search for transiting planets in the WTS light curves, for which we used the Box-Least-Squares (BLS) algorithm, OCCFIT, as described in Aigrain & Irwin (2004), and employed by Miller et al. (2008). The box represents a periodic decrease in the mean flux of the star over a short time scale (an upside-down top hat). The in-occultation data points in the light curves fall into a single bin, I, while the out-of-occultation data points form the ensemble O. This single bin approach may seem simplistic but in the absence of significant intrinsic stellar variability, such as star spot modulation, it becomes a valid approximation to an eclipse and is sufficient for the purpose of *detection*. Given the relatively weak signal induced by star spot activity in the J-band, we did not filter the light curves for stellar variability before executing the detection algorithm. We ran OCCFIT on the M-dwarf sample light curves in the 19h field. Our data invariably suffer from correlated 'red' noise, thus we adjust the OCCFIT detection statistic, S, which assesses the significance of our detections, with the procedure described by Pont et al. (2006) to derive a new statistic, S_{red}. This process is explained in detail for OCCFIT detections in Miller et al. (2008).

3.4.3 Candidate selection

To automatically extract the MEB candidates from results of running OCCFIT on the M-dwarf sample light curves, we required that $S_{\rm red} \geq 5$ and that the detected orbital period must not be near the common window-function alias at one day i.e. $0.99 > P > 1.005$ days. This gave 561 light curves to eyeball, during which we removed objects with spurious eclipse-like features associated with light curves near the saturation limit.

In total, we found 26 sources showing significant eclipse-features in the 19h field, of which 16 appear to be detached and have full-phase coverage, with well-sampled primary and secondary eclipses. The detached MEB candidates are marked on the colour-colour plot in Figure 3.2 by the blue filled circles and red filled squares. The orbital periods of the MEBs corresponding to the blue filled circles are given in Table 3.14 and their folded light curves are shown in Figures 3.13 and 3.14. The MEBs corresponding to the red filled squares are the subjects of the remaining detailed analysis in this paper.

3.5 Low-resolution spectroscopic analysis

Low-resolution spectra of our three characterised MEBs, as shown in Figure 3.3, permit a further analysis of their composite system properties and provide consistency checks on the main-sequence dwarf nature of the systems.

3.5.1 Surface Gravity

Slesnick et al. (2006) and Lodieu et al. (2011) have shown that the depths of alkaline absorption lines between $6300-8825$Å can highlight low surface gravity features in low-mass stars. We used the spectral indices Na_{8189} and TiO_{7140} to search for any giant star contaminants in the MEBs and found that all three MEBs have indices consistent with dwarf star gravity. We note that our low-resolution spectra were not corrected for telluric absorption, which is prevalent in the Na_{8189} region, and thus our measured indices may not be completely reliable. However a visual inspection of the spectra also reveals deep, clear absorption by the NaI doublet at 8183Å, 8195Å as highlighted in Figure 3.3, which is not seen in giant stars. For comparison, we also observed an M4III giant standard star, [R78b] 115, shown at the top of Figure 3.3, with the same set up on the same night. It lacks the deep Na I doublet absorption lines found in dwarfs and its measured spectral indices are $TiO_{7140} = 2.0 \pm 0.2$ and $Na_{8189} = 0.97 \pm 0.04$, which places it in the low-surface gravity region for M4 spectral types in Figure 11 of Slesnick et al. (2006). The gravity-sensitive spectral index values for our MEBs are given in Table 3.7.

3.5.2 Metallicity

The profusion of broad molecular lines in M-dwarf spectra, caused by absorbing compounds such as Titanium Oxide and Vanadium Oxide redwards of 6000Å (Kirkpatrick et al. 1991), make it difficult to accurately define the continuum level, which complicates M-dwarf metallicity measurements. However, recent work shows that the relative strengths of metal hydride and metal oxide molecular bands in low-resolution optical wavelengths can be used to separate metal-poor subdwarfs from solar-metallicity systems. For example, Woolf et al. (2009)

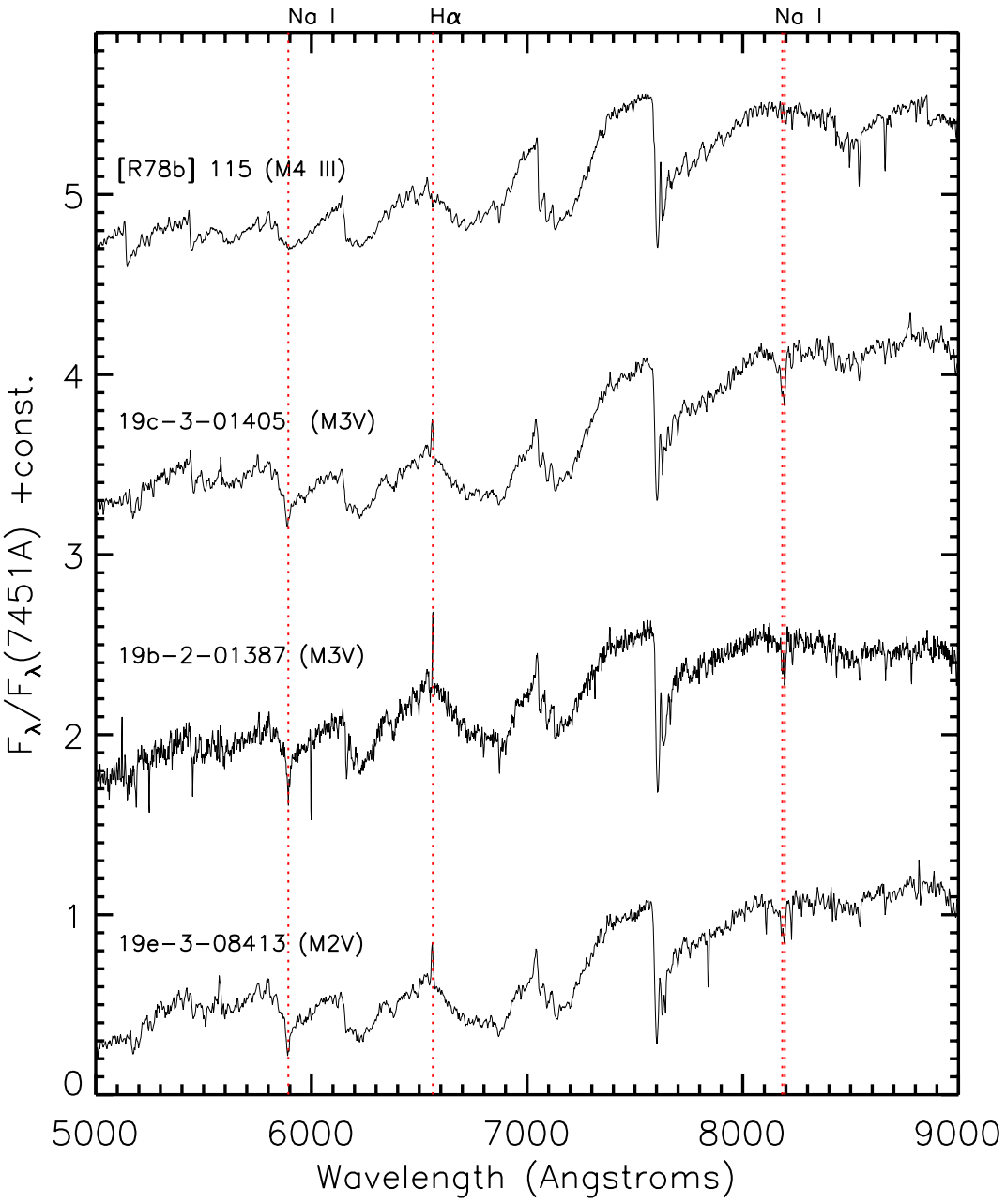

Figure 3.3 — Low-resolution spectra of our three new MEBs plus a known M-giant star (top spectrum) for comparison. The TiO absorption band at 7100Å signifies the onset of the M-dwarf spectral types. The dotted vertical lines, from left to right, mark the Na I, Hα and the Na I doublet rest wavelengths in air. The Na I doublet is strong in dwarfs while the Calcium infrared triplet at 8498, 8542 and 8662Å is strongest in giants. The deep features at 7594 and 7685Å are telluric O_2 absorption. Hα emission is clearly present in all three MEBs.

provided a set of equal metallicity contours in the plane of the CaH2+CaH3 and TiO5 spectral indices defined by Reid et al. (1995), and they mapped the metallicity index $\zeta_{\rm TiO/CaH}$ described by Lépine et al. (2007) onto an absolute metallicity scale, calibrated by metallicity measurements from well-defined FGK stars with M-dwarf companions, albeit with a significant scatter of ~ 0.3 dex. Dhital et al. (2011) have refined the coefficients for $\zeta_{\rm TiO/CaH}$ after finding a slight bias for higher metallicity in early M-dwarfs. We measured the CaH2+CaH3 and TiO5 indices in our MEB spectra and compared them with these works. We found that all three of our systems are consistent with solar metallicity. The measured values of the metallicity-sensitive indices for our MEBs are given in Table 3.7.

One should note that further progress has been made in M-dwarf metallicity measurements by moving to the infrared and using both low-resolution *K*-band spectra (Rojas-Ayala et al. 2010; Muirhead et al. 2011) and high-resolution *J*-band spectra (Önehag et al. 2011; Del Burgo et al. 2011). These regions are relatively free of molecular lines, allowing one to isolate atomic lines (such as Na I and Ca I) and thus achieve a precise continuum placement. However, in the spectra of M-dwarf short period binary systems, one must be aware that the presence of double-lines and rotationally-broadened features further increase the uncertainty in their metallicity estimates.

3.5.3 Hα Emission

All three of our MEBs show clear Hα emission in their low-resolution spectra, although it is not possible to discern if both components are in emission. The equivalent widths of these lines, which are a measure of the chromospheric activity, are reported in Table 3.7, where a negative symbol denotes emission. Hα emission can be a sign of youth, but we do not see any accompanying low-surface gravity features. The strength of the Hα emission seen in our MEBs is comparable with other close binary systems (e.g. Kraus et al. 2011) and thus is most likely caused by high magnetic activity in the systems. None of the systems have equivalent widths < -8Å, which places them in the non-active accretion region of the empirically derived accretion criterion of Barrado y Navascués & Martín (2003).

3.5.4 Spectral type and effective temperature

Our low-resolution spectra permit an independent estimate of the spectral types and effective temperatures of the MEBs to compare with the SED fitting values. Initially, we assessed the spectral types using the HAMMER[5] spectral-typing tool, which estimates MK spectral types by measuring a set of atomic and molecular features (Covey et al. 2007). One can visually inspect the automatic fit by eye and adjust the fit interactively. For the latest-type stars (K and M), the automated characterisation is expected to have an uncertainty of ~ 2 subclasses. We found that 19b-2-01387 has a visual best-match with an M2V system, while the other two MEBs were visually closest to M3V systems. M-dwarf studies (Reid et al. 1995; Gizis 1997) have found that the TiO5 spectral index could also be used to estimate spectral types to an accuracy of ± 0.5 subclasses for stars in the range K7V-M6.5V. The value of this index and the associated spectral

[5]http://www.astro.cornell.edu/∼kcovey/thehammer.html

type (SpT) are given for each of our three MEBs in Table 3.7. We find a reasonable agreement between the spectral index results, the visual estimates and the SED derived spectral types.

Woolf & Wallerstein (2006) derived a relationship between the CaH2 index and the effective temperatures of M-dwarfs in the range 3500K$<$ T_{eff} $<$ 4000 K. Table 3.7 gives the value of this index and the associated effective temperatures, labelled T_{eff} (CaH2), for our three MEBs. Woolf & Wallerstein (2006) do not quote an uncertainty on the relationship, so we assumed errors of $\pm$150 K. Within the assumed errors, the effective temperatures derived from the spectral indices and the SED fitting agree, but the relationship between the CaH2 index and T_{eff} has not been robustly tested for the CaH2 values we have measured.

Instead, we have determined the system effective temperatures for our MEBs by directly comparing the observed spectra to cool star model atmospheres using a χ^2-minimisation algorithm. This incorporated the observational errors, which were taken from the error spectrum produced during the optimal extraction of the spectra. We used a grid of NextGen atmospheric models (Allard et al. 1997) interpolated to the same resolution as our low-resolution spectra. The models had increments of $\Delta T_{eff} = 100$K, solar metallicity and a surface gravity $\log(g) = 5.0$ (a typical value for early-type field M-dwarfs), and spanned $5000 - 8500$Å. During the fitting, we masked out the strong telluric O_2 features at $7594, 7685$Å and the Hα emission line at 6563Å as these are not present in the models, although we found that their inclusion had a negligible affect on the results. All the spectra were normalised to their continuum before fitting. We fitted the χ^2-distribution for each MEB with a six-order polynomial to locate its minimum. The corresponding best-fitting T_{eff} (atmos., adopted) is given in Table 3.7. Assuming systematic correlation between adjacent pixels in the observed spectrum, we multiplied the formal 1σ errors from the χ^2-fit by $\sqrt{3}$ to obtain the final errors on the system effective temperatures.

From here on, our analysis is performed with system effective temperatures derived from model atmosphere fitting. Although our different methods agree within their errors, the model atmosphere fitting is more robust against reddening effects, even if this effect is expected to be small, as discussed earlier.

3.6 Light curve analysis

Light curves of an eclipsing binary provide a wealth of information about the system, including its orbital geometry, ephemeris, and the relative size and relative radiative properties of the stars. We used the eclipsing binary software, JKTEBOP[6] (Southworth et al. 2004b,c), to model the light curves of our MEBs. JKTEBOP is a modified version of EBOP (Eclipsing Binary Orbit Program; Nelson & Davis 1972; Popper & Etzel 1981; Etzel 1980). The algorithm is only valid for well-detached eclipsing binaries with small tidal distortions, i.e near-spherical stars with oblateness < 0.04 (Popper & Etzel 1981). A first pass fit with JKTEBOP showed that this criterion is satisfied by all three of our MEBs.

The light curve model of a detached, circularised eclipsing binary is largely independent of its radial velocity model, which allowed us to perform light curve modelling and derive precise orbital periods on which to base our follow-up multi-wavelength photometry and radial velocity measurements. The RV-dependent part of the light curve model is the mass ratio, q, which controls the deformation of the stars. In our initial analysis to determine precise orbital

[6]http://www.astro.keele.ac.uk/∼jkt/

Name	$T_{\rm eff}$ (SED)	$T_{\rm eff}$ (atmos., adopted)	$T_{\rm eff}$ (CaH2)	SpT (TiO5)	TiO5	CaH2 (Å)
19b-2-01387	3494 ± 116	3590 ± 100	3586 ± 150	M2.7 $\pm$ 0.5	0.52	0.52
19c-3-01405	3389 ± 110	3307 ± 130	3514 ± 150	M2.8 $\pm$ 0.5	0.50	0.48
19e-3-08413	3349 ± 111	3456 ± 140	3569 ± 150	M2.3 $\pm$ 0.5	0.54	0.51

Name	CaH3	TiO_{7140}	Na_{8189}	EW(Hα)
19b-2-01387	0.73	1.46	0.89	-3.2
19c-3-01405	0.75	1.60	0.87	-4.3
19e-3-08413	0.73	1.46	0.90	-4.1

Table 3.7 — A summary of the spectral indices, derived effective temperatures and spectral types (SpT) for the three characterised MEBs. The photometric estimates are labelled with (SED). They have the smallest errors, which include the formal uncertainties plus a 100 K systematic uncertainty, but they potentially suffer from reddening effects and under-estimation of the errors. Our adopted effective temperatures are marked (atmos., adopted). They are derived from comparison with the NextGen model atmosphere spectra (Allard et al. 1997) and are more robust against reddening effects. The (TiO5) and (CaH2) labels mark values derived from the spectral index relations of Reid et al. (1995) and Woolf & Wallerstein (2006), respectively. We use $T_{\rm eff}$ (atmos., adopted) for all subsequent analysis in this paper.

periods, we assumed circular stars, which is reasonable for detached systems, but the observed mass ratios (see Section 3.7) were adopted in the final light curve analysis.

JKTEBOP depends on a number of physical parameters. We allowed the following parameters to vary for all three systems during the final fitting process: i) the sum of the radii as a fraction of their orbital separation, $(R_1 + R_2)/a$, where R_j is the stellar radius and a is the semi-major axis, ii) the ratio of the radii, $k = R_2/R_1$, iii) the orbital inclination, i, iv) the central surface brightness ratio, J, which is essentially equal to the ratio of the primary and secondary eclipse depths, v) a light curve normalisation factor, corresponding to the magnitude at quadrature phase, vi) $e\cos\omega$, where e is the eccentricity and ω is the longitude of periastron, vii) $e\sin\omega$, viii) the orbital period, P and ix) the orbital phase zero-point, T_0, corresponding to the time of mid-primary eclipse. The starting values of P and T_0 are taken from the original OCCFIT detection (see Section 3.4.2). In the final fit, the observed q value is held fixed. The reflection coefficients were not fitted, instead they were calculated from the geometry of the system. The small effect of gravity darkening was determined by fixing the gravity darkening coefficients to suitable values for stars with convective envelopes ($\beta = 0.32$) (Lucy 1967). JKTEBOP will allow for a source of third light in the model, whether it be from a genuine bound object or from some foreground or background contamination, so we initially allowed the third light parameter to vary but found it to be negligible in all cases and thus fixed it to zero in the final analysis.

Our light curves, like many others, are not of sufficient quality to fit for limb darkening, so we fixed the limb darkening coefficients for each component star. JKTLD is a subroutine of JKTEBOP that gives appropriate limb darkening law coefficients for a given bandpass based on a database of coefficients calculated from available stellar model atmospheres. We used the PHOENIX model atmospheres (Claret 2000, 2004) and the square-root limb darkening law in all cases. Studies such as van Hamme (1993) have shown that the square-root law is the most accurate at infrared wavelengths. For each star, we assumed surface gravities of $\log(g) = 5$, a

Parameter	19b-2-01387	19c-3-01405	19e-3-08413
WTS J-band			
P (days)	1.49851768	4.9390945	1.67343720
	$\pm$0.00000041	$\pm$0.0000015	$\pm$0.00000048
T_0 (HJD)	245332.889802	245393.80791	245374.80821
	$\pm$0.000077	$\pm$0.00022	$\pm$0.00016
(R_1+R_2)/a	0.17818 ± 0.00040	0.07023 ± 0.00035	0.1544 ± 0.0016
k	0.967 ± 0.044	0.987 ± 0.081	0.782 ± 0.070
J	0.9307 ± 0.0043	0.993 ± 0.013	0.8162 ± 0.0084
i ($^\circ$)	88.761 ± 0.051	89.741 ± 0.053	87.59 ± 0.26
$e\cos\omega$	-0.00020 ± 0.00017	0.000060 ± 0.000068	-0.00014 ± 0.00017
$e\sin\omega$	-0.0007 ± 0.0026	-0.0041 ± 0.0059	0.0112 ± 0.0062
Norm.(mag)	14.64726 ± 0.00017	0.00003 ± 0.00020	15.22776 ± 0.00020
R_1/a	0.0906 ± 0.0020	0.0354 ± 0.0014	0.0867 ± 0.0027
R_2/a	0.0875 ± 0.0021	0.0348 ± 0.0015	0.0676 ± 0.0040
L_2/L_1	0.871 ± 0.076	0.97 ± 0.15	0.503 ± 0.090
e	0.0066 ± 0.0026	0.0058 ± 0.0043	0.0114 ± 0.0062
ω ($^\circ$)	268.0 ± 1.7	180.5 ± 90.9	91.1 ± 1.2
σ_J (mmag)	5.2	8.4	8.7
INT i-band			
J	0.8100	—	0.63
σ_i (mmag)	5.7	—	12.1
IAC80 g-band			
J	—	—	0.6455
σ_i (mmag)	—	—	29.9

Table 3.8 — Results from the J and i-band light curve analysis. Only perturbed parameters are listed. The light curve parameter errors are the 68.3% confidence intervals while the model values are the means of the 68.3% confidence level boundaries, such that the errors are symmetric. T_0 corresponds to the epoch of mid-primary eclipse for the first primary eclipse in the J-band light curve. Errors on 19e-3-08413 are from residual permutation analysis as they were the largest, indicating time-correlated systematics. $\sigma_{J,i}$ give the RMS of the residuals to the final solutions, where all parameters in the fit are fixed to the quoted values and the reflection coefficients calculated from the system geometry.

solar metallicity and micro-turbulence of 2 km/s, and used estimated effective temperatures for the component stars: $[T_{\rm eff,1}, T_{\rm eff,2}]$ =[3500K, 3450K] for 19b-2-01387, $[T_{\rm eff,1}, T_{\rm eff,2}]$ =[3300K, 3300K] for 19e-3-08413, and $[T_{\rm eff,1}, T_{\rm eff,2}]$ =[3525K, 3350K] for 19c-3-01405. Note that we did not iterate the limb darkening coefficients with the final derived values of T_1 and T_2 (see Section 3.8) as they only differed by ~ 30 K ($< 1\sigma$) from the assumed values. This would be computationally intensive to do and would result in a negligible effect on the final result.

The phase-folded J-band light curves for the MEBs and their final model fits are shown in Figures 3.4, 3.5 and 3.6, while the model values are given in Table 3.8.

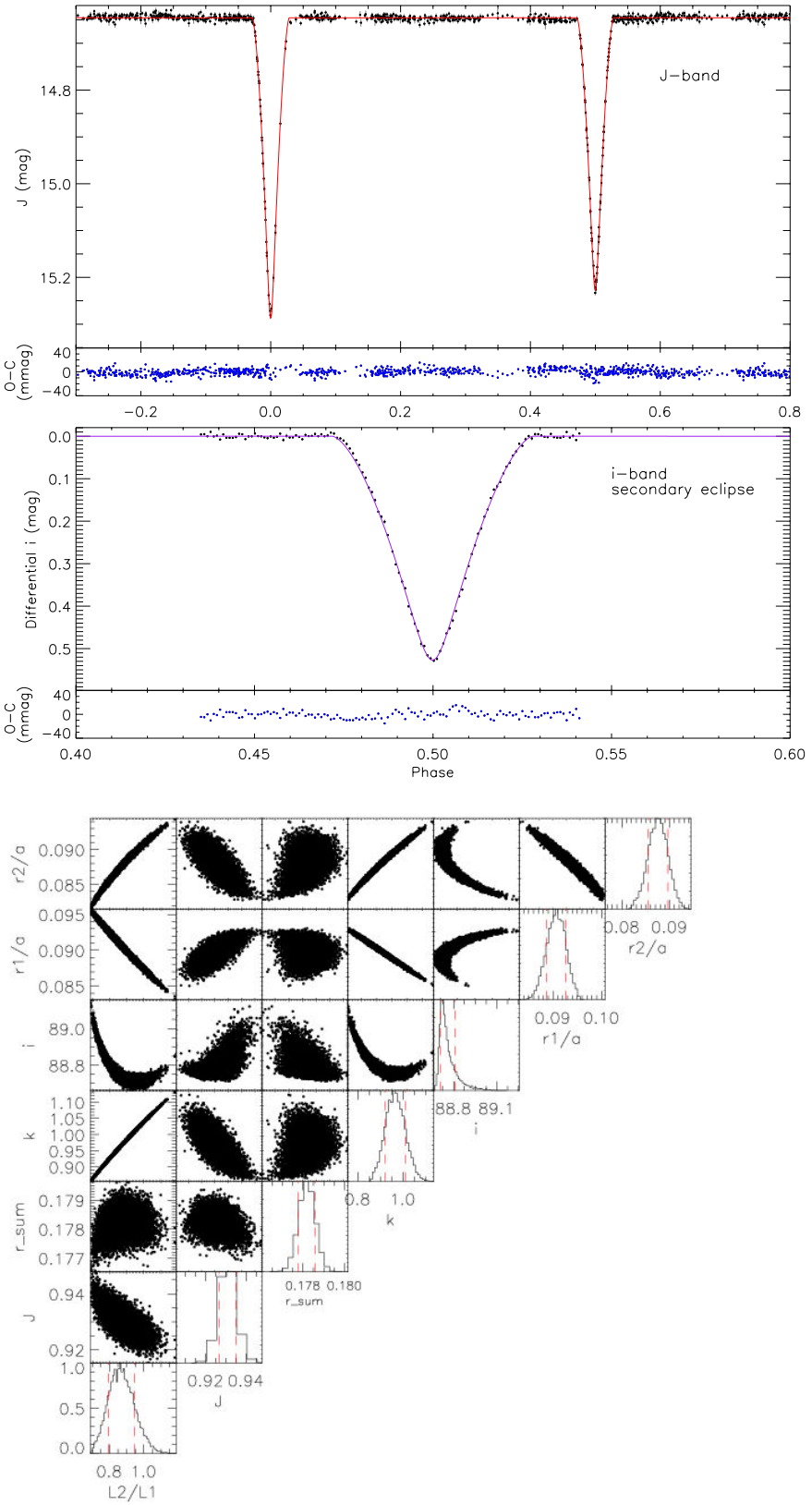

Figure 3.4 — 19b-2-01387 Top panel: full phase WFCAM *J*-band light curve. Middle panel: the INT/WFC *i*-band light curve at secondary eclipse. The solid red and purple lines show the best-fit from JKTEBOP. The blue data points in the smaller panels show the residuals after subtracting the model. Bottom panel: Parameter correlations from Monte Carlo simulations and histograms of individual parameter distributions. The red dashed vertical lines mark the 68.3% confidence interval. For a high resolution plot please refer to the online paper.

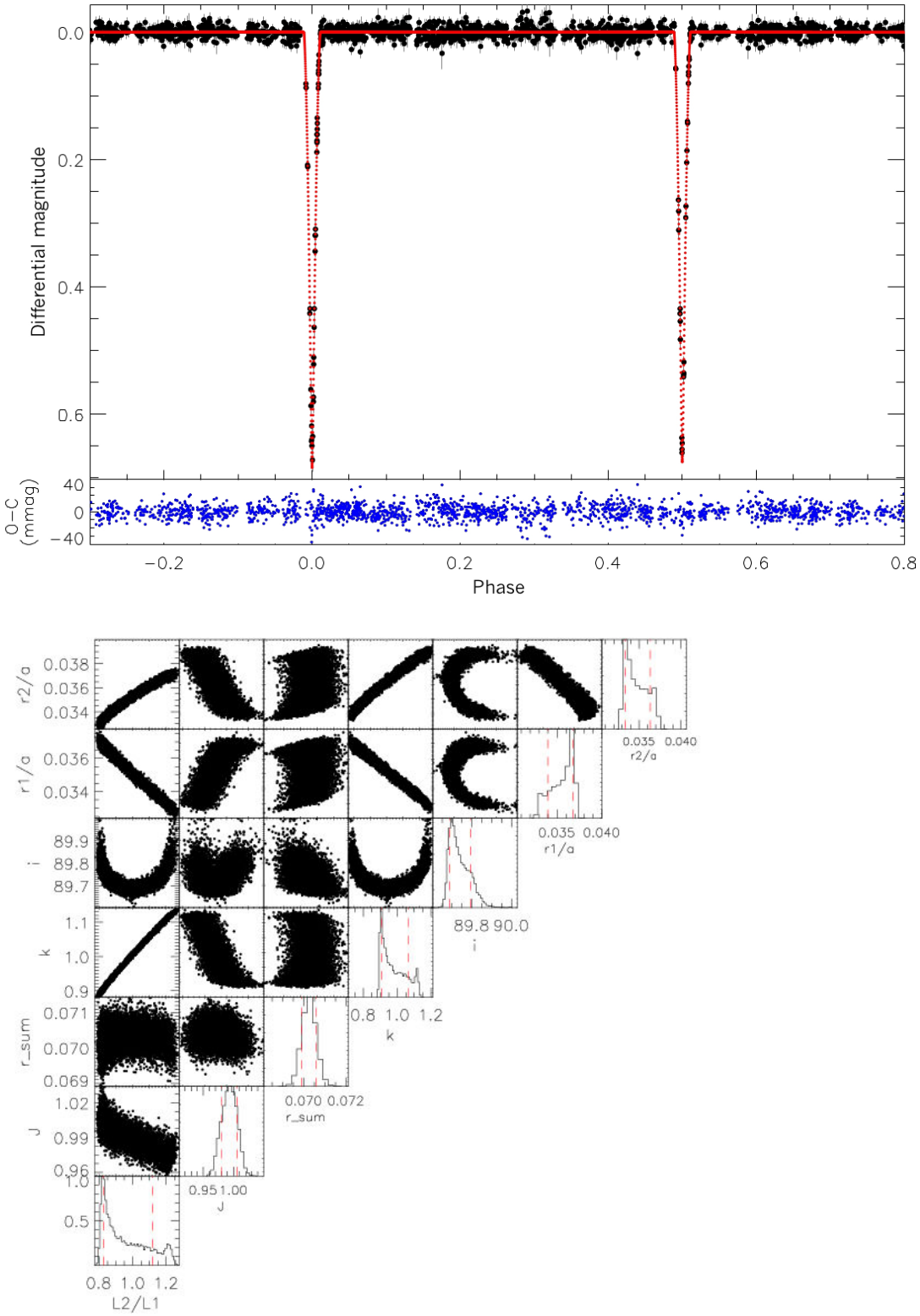

Figure 3.5 — 19c-3-01405 Top panel: WFCAM *J*-band light curve. Lines and panels as in Figure 3.4. The magnitude scale is differential as we have combined light curves from two different WFCAM chips. Bottom panel: Monte Carlo results with lines as in Figure 3.4. Our inability to constrain the model with follow-up data results in strong correlation between the radius ratio and light ratio and parameter distributions that are significantly skewed. There are also degeneracies in the inclination which is expected given the near identical eclipse depths. For a high resolution MCMC plot please refer to the online paper.

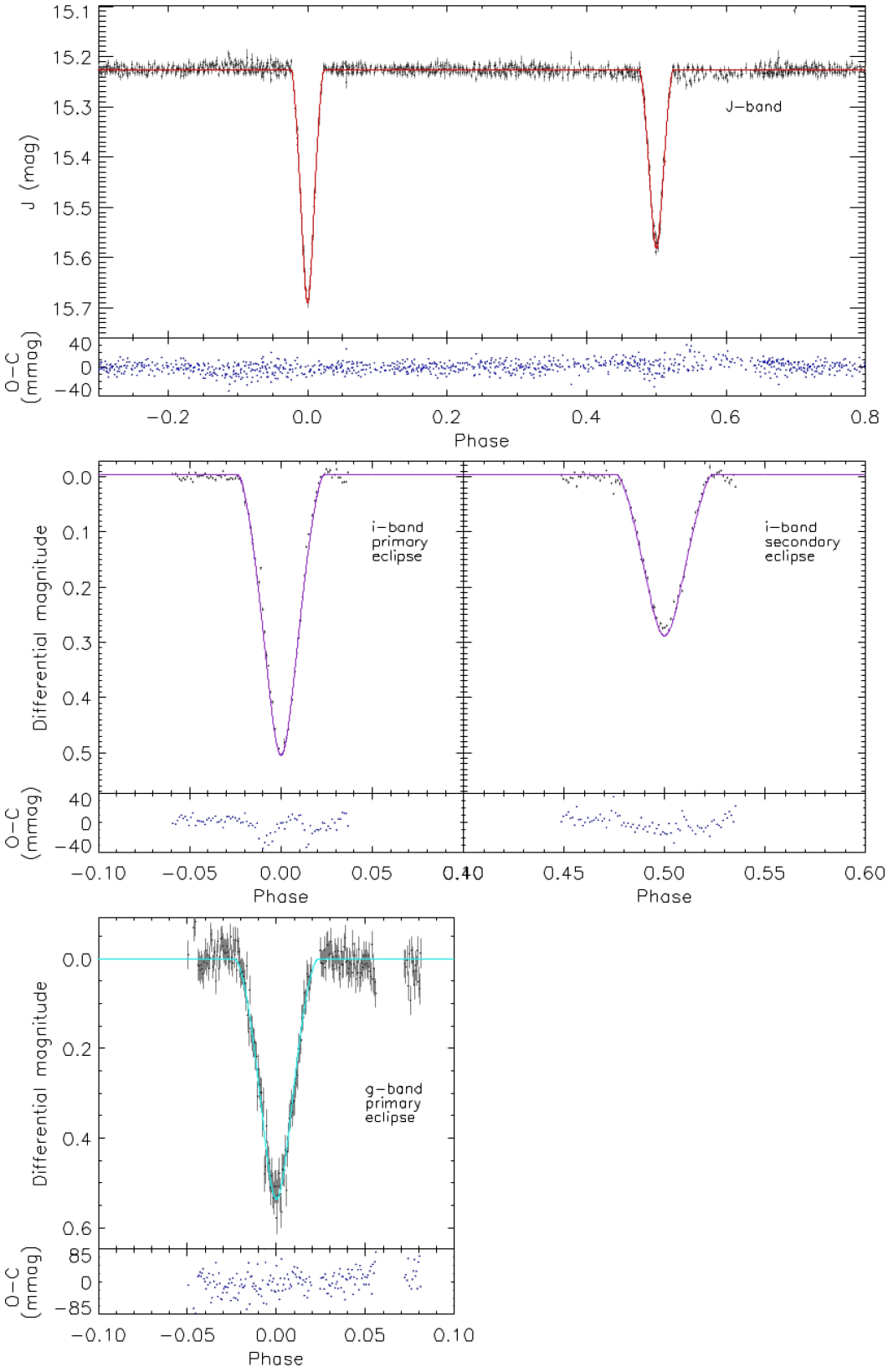

Figure 3.6 — 19e-3-08413 Top panel: full phase WFCAM *J*-band light curve. Middle panels: INT/WFC *i*-band light curves of a primary and a secondary eclipse. Bottom panel: IAC80 *g*-band light curve of a primary eclipse. The solid red, purple, and cyan lines show the best-fit from JKTEBOP. For a high resolution MCMC plot please refer to the online paper. Parameter correlations from residual permutations, which gave the larger errors on the model parameters than the Monte Carlo simulations, indicating time-correlated systematics. There are strong correlations between the light ratio, radius ratio and inclination.

3.6.1 Error analysis

JKTEBOP uses a Levenberg–Marquardt minimisation algorithm (Press et al. 1992) for least-squares optimisation of the model parameters; however, the formal uncertainties from least-squares solutions are notorious for underestimating the errors when one or more model parameters are held fixed, due to the artificial elimination of correlations between parameters. JKTEBOP provides a method for assessing the 1σ uncertainties on the measured light curve parameters through Monte Carlo (MC) simulations. In these simulations, a synthetic light curve is generated using the best-fitting light curve model at the phases of the actual observations. Random Gaussian noise is added to the model light curve which is then fitted in the same way as the data. This process is repeated many times and distribution of the best fits to the synthetic light curves provide the 1σ uncertainties on each parameter. Southworth et al. (2005b) showed this technique is robust and gives similar results to Markov Chain Monte Carlo techniques used by others, under the (reasonable) assumption that the best fit to the observations is a good fit. JKTEBOP can also perform a residual permutation (prayer bead) bead error analysis which is useful for assigning realistic errors in the presence of correlated noise (Southworth 2008). For each MEB, we have performed both MC simulations (using $10,000$ steps) and a prayer bead analysis. The reported errors are those from the method that gave the largest uncertainties. The correlations between the parameter distributions from the MC and prayer bead analysis are shown in Figures 3.4, 3.5 and 3.6 along with histograms of the distributions of individual parameters. The distributions are not perfectly Gaussian and result in asymmetric errors for the 68.3% confidence interval about the median. As we wish to propagate these errors into the calculation of absolute dimension, we have symmetrized the errors by adopting the mean of the 68.3% boundaries (the 15.85% and 84.15% confidence limits) as the parameter value and quoting the 68.3% confidence interval as the $\pm1\sigma$ errors. These errors are given in Table 3.8 for each MEB.

Our follow-up g- and i-band light curves (where available) were used to check the J-band solution by modelling them with the derived J-band parameters, but allowing the surface brightness ratio and the light curve normalisation factor to vary. The limb darkening coefficients were changed to those appropriate for the respective g- and i-band and the reflection coefficients were again determined by the system geometry. The RMS values of the these fits are given in Table 3.8 along with the derived g- and i-band surface brightness ratio for completeness. The g- and i-band phase-folded data is shown overlaid with the models in Figure 3.4 and 3.6. We find that the J-band solutions are in good agreement with the $g-$ and i-band data.

3.6.2 Light ratios

All three of our MEBs exhibit near equal-depth eclipses, implying that the systems have components with similar mass. This is promising because it suggest relatively large reflex motions that will appear as well-separated peaks in a cross-correlation function from which we derive RVs. However, it is well-known for systems with equal size components that the ratio of the radii, which depends on the depth of the eclipses, is very poorly determined by the light curve (Popper 1984), even with the high photometric precision and large number epochs in the WTS (see Andersen et al. (1980); Southworth et al. (2007a) for other excellent examples of this phenomenon). Conversely, $(R_1 + R_2)/a$, is often very well-constrained because it depends mainly

on the duration of the eclipses and the orbital inclination of the system. The reason that the ratio of the radii is so poorly constrained stems from the fact that quite different values of R_2/R_1 result in very similar eclipse shapes.

Unfortunately, we found that all three of our MEBs presented problems associated with poorly constrained R_2/R_1, revealed in the initial modelling as either a large skew in the errors on the best-fit parameters or best-fit solutions that were physically implausible. For example, for 19b-2-01387, the initial best-fit gave $L_2/L_1 > 1$ and $R_2/R_1 > 1$ while $T_2/T_1 < 1$. We know from our low-resolution spectroscopy that these stars are very likely to be ordinary main-sequence M-dwarfs and while their exact radii may be under-estimated by models, they generally obey the trend that less massive stars are less luminous, smaller and cooler. We note that Stassun et al. (2007) found a temperature reversal in a system of two young brown dwarfs where the less massive component was hotter but smaller and fainter than its companion. In their case the more massive component, although cooler, had an RV curve and eclipse depth that were consistent. In our cases, the most massive component (smallest $K_\star$) comes towards us (blue-shift) after the deepest (primary) eclipse, so it must be the more luminous component. The uncertainty in our modelling is most likely to due to insufficient coverage of the mid-eclipse points.

However, we can try to use external data as an additional constraint in the fit. Some authors employ a spectroscopically derived light ratio as an independent constraint on k in the light curve modelling (Southworth et al. 2004a, 2007b; Nordstrom & Johansen 1994). JKTEBOP allows the user to incorporate an input light ratio in the model and propagates the errors in a robust way. The input light ratio adds a point in the flux array at a specific phase (Southworth et al. 2007b). If this is supplied with a very small error, the point is essentially fixed. We have tried several methods to estimate the light ratio for each of our three systems, although we stress here that none of the estimates should be considered as significant. One requires high resolution spectra to extract precise light ratios, via the analysis of the equivalent width ratios of metallic lines, which will be well-separated if observed at quadrature (Southworth et al. 2005b). With a high resolution spectrum, one can disentangle the components of the eclipsing binary and perform spectral index analysis on the separate components (e.g. Irwin et al. 2007a).

19b-2-01387 is our brightest system and subsequently has the highest signal-to-noise in our intermediate-resolution spectra. The best spectrum is from the first night of observations. For this system, we estimated the light ratio in three ways: i) by measuring the ratio of the equivalent widths of the lines in the Na II doublet (shown in Figure 3.7), ii) by using the two-dimensional cross-correlation algorithm, TODCOR (Zucker & Mazeh 1994), which weights the best-matching templates by the light ratio and, iii) by investigating the variation in the goodness-of-fit for a range of input light ratios in the model.

For the first method, the IRAF.SPLOT task was used to measure the equivalent width of the Na I doublet feature with rest wavelength 8183.27Å for each star. Note that this assumes the components have the same effective temperature. The ratio was $EW(2)/EW(1) = 0.3582/0.4962 = 0.7219$. In the second method, we found that only the spectrum from the first night contained sufficient SNR to enable TODCOR to correctly identify the primary and secondary components. It is known that TODCOR does not perform as well for systems with similar spectral features (Southworth & Clausen 2007) so we do not use it to derive RVs for our nearly equal mass systems. The TODCOR estimated light ratio was $L_2/L_1 = 0.846$. In the final method, we iterated JKTEBOP across a grid of initial light ratios between 0.6-1.1, in steps

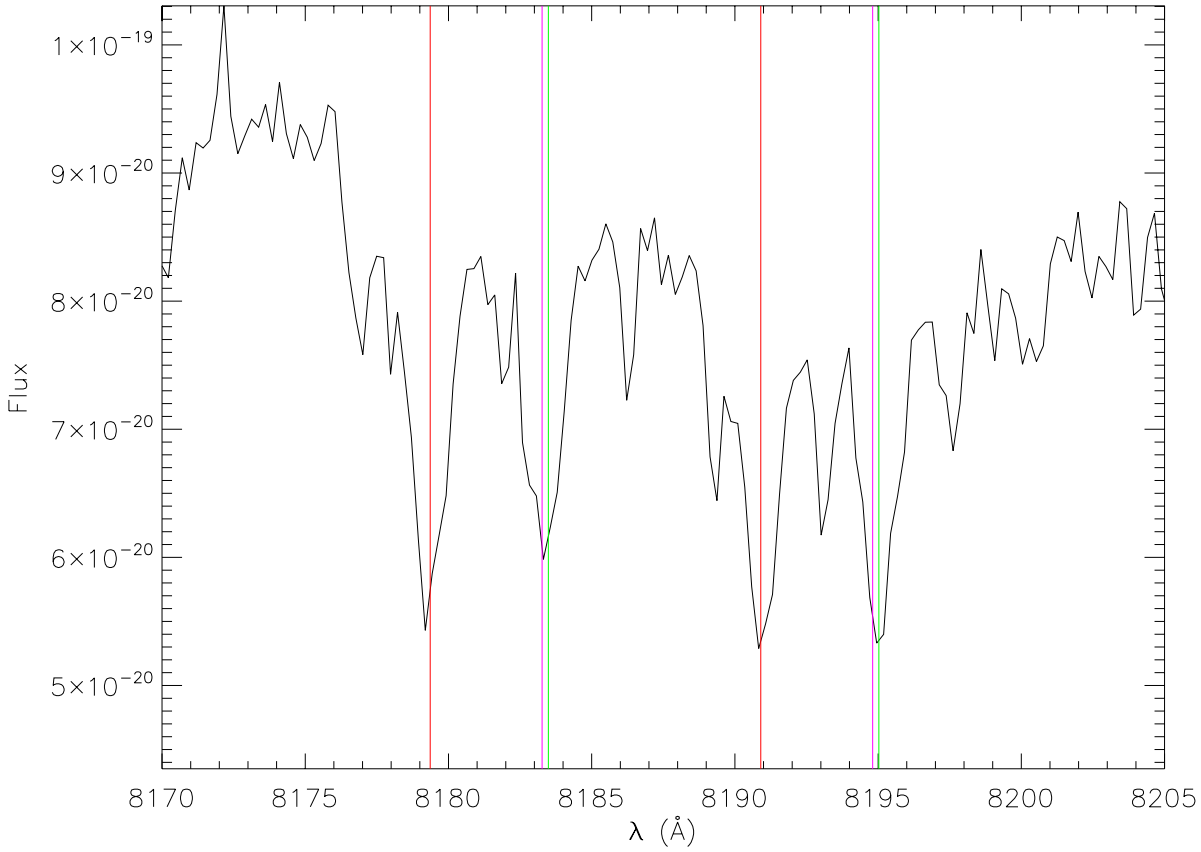

Figure 3.7 — 19b-2-01387: A high signal-to-noise intermediate resolution spectrum taken near quadrature phase of 19b-2-01387 in the Na II doublet wavelength region which we used to measure equivalents widths to estimate the light ratio. The purple vertical lines show the rest frame wavelength of the doublet at λ8183.27Å, λ8194.81Å. The red lines mark the doublet for primary object and the green lines mark the secondary doublet lines, based on the RVs derived in Section 3.7.

of 0.01, with very small errors while allowing all our usual parameters to vary. The resulting χ^2-distribution is not well-behaved. There is a local and global minimum at $L_2/L_1 = 0.72$ and $L_2/L_1 = 0.97$, respectively, but the global minimum is bracketed on one side by a significant jump to a much larger χ^2 suggesting numerical issues. We opted to use the light ratio derived with TODCOR as the input to the model. This value lies half-way between the two minimums of the χ^2 distribution, so we supplied it with a $\sim 15\%$ error to allow the parameter space to be explored, given the uncertainty in our the measurement. Our follow-up *i*-band data of a single secondary eclipse also prefers a light ratio less than unity, but the lack of phase coverage does not give a well-constrained model. The resulting parameter distributions, shown in Figure 3.4, show strong correlation between the light ratio and R_2/R_1 as expected. The resulting 1σ error boundary for the light ratio, which is computed from k and J, is in broad agreement with the methods used to estimate it.

For 19e-3-08413, we obtained additional *i*-band photometry of a primary and secondary eclipse, plus a further primary eclipse in the *g*-band. Here, we have estimated the light ratio

by fitting our two datasets in these wavebands separately, using appropriate limb darkening coefficients for the *i*- and *g*-bands in each case, and allowing all our usual parameters to vary. We find best-fit values from the *i*- and $g-$bands of $L_2/L_1 = 0.29$ and $L_2/L_1 = 0.36$, respectively. This confirms a light ratio less than unity, but as the light ratio depends on the surface brightness ratio, which in turn is wavelength dependent, we adopted $L_2/L_1 = 0.29$ with input with an error of ± 0.5 in the final fit to the *J*-band data. Note we chose to use the *i*-band value as it is closer in wavelength to the *J*-band and the light curve was of higher quality.

In the case of 19c-3-01405, we could not derive a light ratio from the low SNR spectra, nor do we have follow-up *i*-band photometry (due to time scheduling constraints). The eclipses are virtually identical so we supplied an input light ratio of $L_2/L_1 = 1.0$ with an error of 50%. Unfortunately, the final error distributions for the parameters are still quite skewed, as shown in Figure 3.5.

3.6.3 Star spots

For 19e-3-08413, we found that the residual permutation analysis gave larger errors, indicating time-correlated systematics. We have not allowed for spot modulation in our light curve model thus the residuals systematics may have a stellar origin. As mentioned previously, we expect star spot modulation in the *J*-band to be relatively weak as the SED of the spot and the star at these wavelength are more similar than at shorter wavelengths. It is difficult to test for the presence of spots in the *g*- and *i*-band data as we do not have suitable coverage out-of-eclipse. We only have full-phase out-of-eclipse observations in a single *J*-bandpass therefore any physical spot model will be too degenerate between temperature and size to be useful. Furthermore, our *J*-band data span nearly four years, yet spot size and location are expected to change on much shorter timescales, which leads to a change in the amplitude and phase of their sinusoidal signatures. Stable star spot signatures over the full duration of our observations would be unusual. The WTS observing pattern therefore makes it difficult to robustly fit simple sinusoids, as one would need to break the light curve into many intervals in order to have time spans where the spots did not change significantly (e.g. three week intervals), and these would consequently consist of few data points. Nevertheless, we have attempted to test for spot modulation in a very simplistic manner by fitting the residuals of our light curve solutions as a function of time (t) with the following sinusoid:

$$f(t) = a_0 + a_1 \sin(2\pi(t/a_2) + a_3), \tag{3.1}$$

where the systemic level (a_0), amplitude (a_1), and phase (a_3) were allowed to vary in the search for the best-fit, while the period (a_2) was held fixed at the orbital period as we expect these systems to be synchronised (see Table 3.11 for the theoretical synchronisation timescales). Once the best-fit was found, the values were used as starting parameters for the IDL routine MPFITFUN, to refine the fit and calculate the errors on each parameter. Table 3.9 summarises our findings.

There is evidence to suggest a low-level synchronous sinusoidal modulation in 19b-2-01387 and 19e-3-08413 with amplitude $\sim 1.8-3.5$ mmag, but we do not find significant modulation for our longest period MEB (19c-3-01405). The modulation represents a source of systematic error that if modelled and accounted for, could reduce the errors our radius measurements.

Name	Amplitude (mmag)	Phase	γ (mmag)	$\chi^2_{\nu,\mathrm{before}}$	$\chi^2_{\nu,\mathrm{after}}$	$\mathrm{RMS}_{\mathrm{before}}$ (mmag)	$\mathrm{RMS}_{\mathrm{after}}$ (mmag)
19b-2-01387	1.83 ± 0.23	2.53 ± 0.012	0.19 ± 0.15	1.11	1.04	5.2	4.9
19c-3-01405	0.22 ± 0.27	-1.5 ± 1.3	0.23 ± 0.20	0.87	0.87	8.4	8.4
19e-3-08413	3.47 ± 0.32	-0.143 ± 0.050	0.39 ± 0.22	1.32	1.19	7.8	7.5

Table 3.9 — Results of modelling the light curve model residuals with the simple sinusoid defined by Equation 3.1, to test for the presence of spot modulation. The terms 'before' and 'after' refer to the reduced χ^2 and RMS values before subtracting the best-fit sine curve and then after the subtraction. Note: mmag = 10^{-3} mag. The $\mathrm{RMS}_{\mathrm{before}}$ value for 19e-3-08413 is different to Table 3.8 as one data point was clipped due to it being a significant outlier.

However, with only one passband containing out-of-eclipse variation, we cannot provide a useful non-degenerate model. Good-quality out of eclipse monitoring is required and given that spot modulation evolves, contemporaneous observations are needed, preferably taken at multiple wavelengths to constrain the spot temperatures (Irwin et al. 2011). It is surprising that the apparent spot modulation in our MEBs persists over the long baseline of the WTS observations and perhaps an alternate explanation lies in residual ellipsoid variations from tidal effects between the two stars. We note here that our limiting errors in comparing these MEBs to the mass-radius relationship in Section 3.9.1 are on the masses, not the radii.

3.7 Radial velocity analysis

To extract the semi-amplitudes (K_1, K_2) and the centre-of-mass (systemic) velocity, γ, of each MEB system, we modelled the RV data using the IDL routine MPFITFUN (Markwardt 2009), which uses the Levenberg–Marquardt technique to solve the least-squares problem. The epochs and periods were fixed to the photometric solution values as these are extremely well-determined from the light curve. Circular orbits were assumed ($e = 0$) for all three systems as the eccentricity was negligible in all light curve solutions. We fitted the primary RV data first using the following model:

$$RV_1 = \gamma - K_1 \sin(2\pi\phi) \tag{3.2}$$

where ϕ is the phase, calculated from the light curve solution, and K is the semi-amplitude. To obtain K_2, we then fitted the secondary RV data points using the equation above, but this time fixed γ to the value determined from the primary RV data.

$$RV_2 = \gamma + K_2 sin(2\pi\phi) \tag{3.3}$$

The errors on each RV measurement are weighted by the RV error given by IRAF.FXCOR and then scaled until the reduced χ^2 of the model fit is unity. The RMS of the residuals is quoted alongside the derived parameters in Table 3.10, and is treated as the typical error on each RV data point. The RMS ranges from $\sim 2-5$ km/s between the systems and for the

Parameter	19b-2-01387	19c-3-01405	19e-3-08413
K_1 (km/s)	90.7 ± 1.6	55.2 ± 2.2	72.1 ± 2.0
K_2 (km/s)	94.0 ± 2.3	60.2 ± 1.4	95.2 ± 3.0
γ (km/s)	-70.7 ± 1.3	-4.8 ± 2.0	43.8 ± 1.8
RMS_1 (km/s)	1.8	3.7	2.7
RMS_2 (km/s)	5.4	2.5	5.0
q	0.965 ± 0.029	0.917 ± 0.042	0.757 ± 0.032
$a \sin i$ ($R_\odot$)	5.472 ± 0.083	11.27 ± 0.25	5.53 ± 0.12
$M_1 \sin^3 i$ ($M_\odot$)	0.498 ± 0.019	0.410 ± 0.021	0.462 ± 0.025
$M_2 \sin^3 i$ ($M_\odot$)	0.480 ± 0.017	0.376 ± 0.023	0.350 ± 0.018

Table 3.10 — Results from radial velocity analysis.

given magnitudes of our systems is the same as the predictions of Aigrain et al. (2007) who calculated the limiting RV accuracy for ISIS on the WHT, when using 1 hour exposures and an intermediate resolution grating centred on 8500Å.

The RV curves for the primary and secondary components of the three MEBs are shown in Figure 3.8 along with the residuals of each fit. The error bars are the scaled errors from IRAF.FXCOR and serve as an indicator of the signal-to-noise in the individual spectra and the degree of mismatch with the best template.

3.8 Absolute dimensions and space velocities

Combining the results of the light curve and RV curve modelling allows us to derive the absolute masses and radii of our MEB components. Table 3.11 gives these dimensions along with the separations, individual effective temperatures, surface gravities, and bolometric luminosities for each binary system. The masses and radii lie within the ranges $0.35-0.50 M_\odot$ and $0.37-0.5 R_\odot$ respectively, and span orbital periods from $1-5$ days. The derived errors on the masses and radii are $\sim 3.5-6.4\%$ and $\sim 2.7-5.5\%$, respectively.

Eclipsing binaries are one of the first rungs on the Cosmic Distance Ladder and have provided independent distance measurements within the local group e.g. to the Large Magellanic Cloud and to the Andromeda Galaxy (Guinan et al. 1998; Ribas et al. 2005; Bonanos 2007). The traditional method for measuring distances to eclipsing binaries is to compute the bolometric magnitude using the luminosity, radius and effective temperature found from the light curve and RV curve analysis. This is combined with a bolometric correction and the system apparent magnitude to compute the distance. While this can yield quite accurate results, the definitions for effective temperature and the zero points for the absolute bolometric magnitude and the bolometric correction must be consistent (Bessell et al. 1998; Girardi et al. 2002). However, we have opted to use a different method to bypass the uncertainties attached to bolometric corrections. We used JKTABSDIM (Southworth et al. 2005a), a routine that calculates distances using empirical relations between surface brightness and effective temperature. These relations are robustly tested for dwarfs with $T_{\rm eff} > 3600$ K and there is evidence that they are valid in the infrared to ~ 3000 K (Kervella et al. 2004). The scatter around the calibration of the relations in the infrared is on the 1% level. The effective temperature scales used for the EB analysis

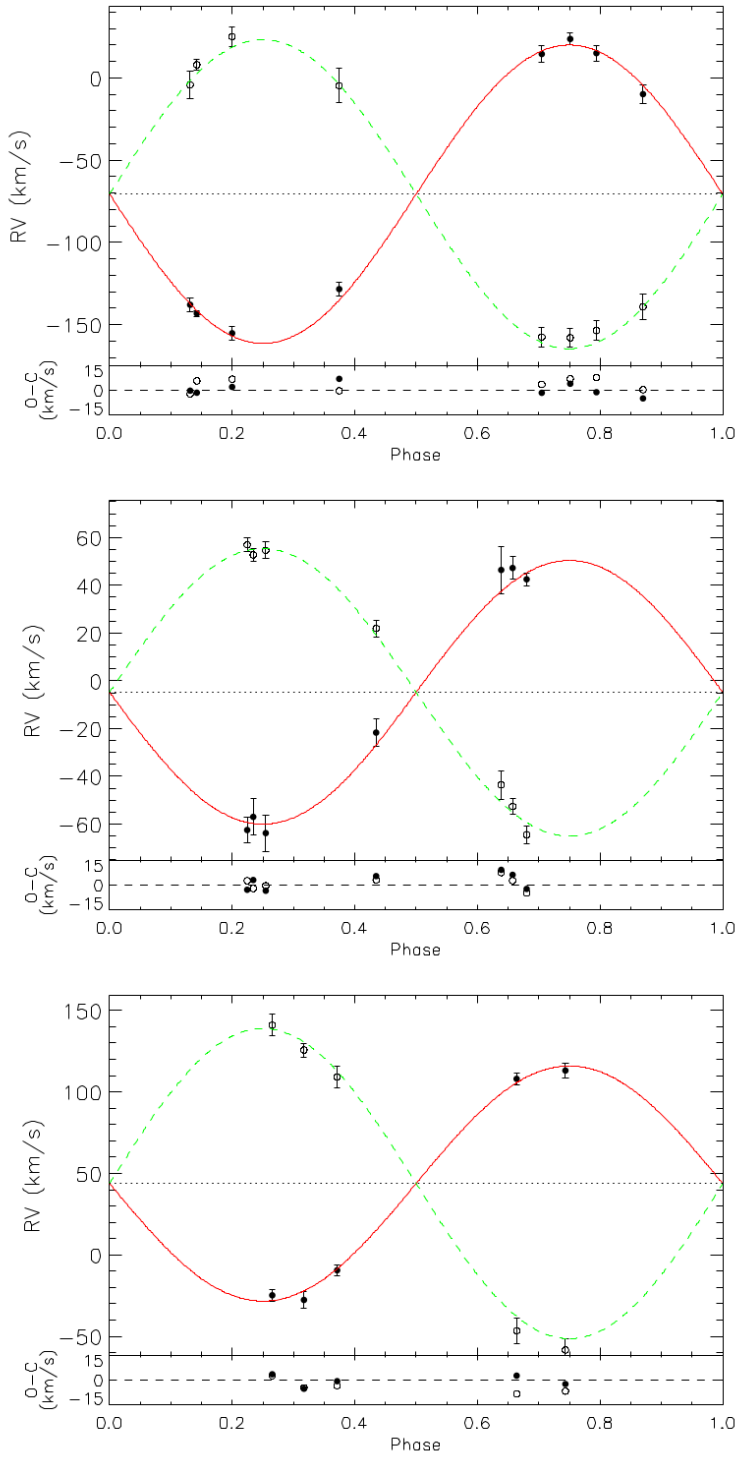

Figure 3.8 — Primary and secondary RV curves for the MEBs. Top: **19b-2-01387**; Middle: **19c-3-01405**; Bottom: **19e-3-08413**. The solid black circles are RV measurements for the primary star, while open circles denote the secondary star RV measurements. The solid red lines are the model fits to the primary RVs and the dashed green lines are the fits to the secondary RVs, fixed to the systemic velocity of their respective primaries. The horizontal dotted lines mark the systemic velocities. The error bars are from IRAF.FXCOR but are scaled so that the reduced χ^2 of the model fit is unity. They are merely an indication of the signal-to-noise of the individual spectra and the mismatch between the template and data. Under each RV plot is a panel showing the residuals of the best-fits to the primary and secondary RVs. Note the change in scale for the y-axis. The typical RV error for each component is given in Table 3.10 by the RMS of their respective residuals.

Parameter	19b-2-01387	19c-3-01405	19e-3-08413
M_1 ($M_\odot$)	0.498 ± 0.019	0.410 ± 0.023	0.463 ± 0.025
M_2 ($M_\odot$)	0.481 ± 0.017	0.376 ± 0.024	0.351 ± 0.019
R_1 ($R_\odot$)	0.496 ± 0.013	0.398 ± 0.019	0.480 ± 0.022
R_2 ($R_\odot$)	0.479 ± 0.013	0.393 ± 0.019	0.375 ± 0.020
a ($R_\odot$)	5.474 ± 0.083	11.27 ± 0.27	5.54 ± 0.12
$\log(g_1)$	4.745 ± 0.039	4.851 ± 0.055	4.742 ± 0.053
$\log(g_2)$	4.760 ± 0.035	4.825 ± 0.064	4.834 ± 0.051
$T_{\rm eff,1}$ (K)	3498 ± 100	3309 ± 130	3506 ± 140
$T_{\rm eff,2}$ (K)	3436 ± 100	3305 ± 130	3338 ± 140
$L_{\rm bol,1}(L_\odot)$	0.0332 ± 0.0042	0.0172 ± 0.0031	0.0314 ± 0.0058
$L_{\rm bol,2}(L_\odot)$	0.0289 ± 0.0037	0.0166 ± 0.0031	0.0167 ± 0.0033
$M_{\rm 1,bol}$	8.45 ± 0.14	9.16 ± 0.20	8.51 ± 0.19
$M_{\rm 2,bol}$	8.60 ± 0.14	9.20 ± 0.20	9.26 ± 0.23
$V_{\rm 1rot,sync}$ (km/s)	16.73 ± 0.45	4.08 ± 0.19	14.51 ± 0.55
$V_{\rm 2rot,sync}$ (km/s)	16.73 ± 0.45	4.01 ± 0.20	11.31 ± 0.70
$t_{\rm sync}$ (Myrs)	0.05	6.3	0.1
$t_{\rm circ}$ (Myrs)	2.6	1480	4.0
$d_{\rm adopted}$ (pc)	545 ± 29	645 ± 53	610 ± 52
U (km/s)	-63.6 ± 7.0	-2.4 ± 9.0	30.9 ± 8.6
V (km/s)	1.0 ± 7.8	1.3 ± 12.2	-10.2 ± 11.8
W (km/s)	-37 ± 6.4	-4.2 ± 8.5	30.1 ± 8.1

Table 3.11 — Derived properties for the three MEBs. $V_{\rm rot,sync}$ are the rotational velocities assuming the rotation period is synchronised with the orbital period. $t_{\rm sync}$ and $t_{\rm circ}$ are the theoretical tidal synchronisation and circularisation timescales from Zahn (1975, 1977)

and the calibration of its relation with surface brightness should be the same to avoid systematic errors but this is a more relaxed constraint than required by bolometric correction methods (Southworth et al. 2005a). The infrared J,H and K-bands are relatively unaffected by interstellar reddening but we have shown in Section 3.4.1 that we expect a small amount. In the distance determination, we have calculated the distances at zero reddening and at the maximum reddening ($E(B-V) = 0.103$ at 1 kpc for early M-dwarfs with $J \leq 16$ mag). Our adopted distance, $d_{\rm adopted}$, reported in Table 3.11 is the mid-point of the minimum and maximum distance values at the boundaries of their the individual errors, which includes the propagation of the effective temperature uncertainties. The MEBs lie between $\sim 550 - 650$ pc.

With a full arsenal of kinematic information (distance, systemic velocities, proper motions and positions) we can now derive the true space motions, UVW, for the MEBs and determine whether they belong to the Galactic disk or halo stellar populations. We used the method of Johnson & Soderblom (1987) to determine UVW values with respect to the Sun (heliocentric) but we adopt a left-handed coordinate system to be consistent with the literature, that is, U is positive away from the Galactic centre, V is positive in the direction of Galactic rotation and W is positive in the direction of the north Galactic pole. We use the prescription of Johnson & Soderblom (1987) to propagate the errors from the observed quantities and the results are summarised in Table 3.11.

Figure 3.9 shows the MEBs in relation to the error ellipse for the Galactic young disk as defined by Leggett (1992) ($-20 < U < 50$, $-30 < V < 0$, $-25 < W < 10$ w.r.t the Sun). 19c-3-01405 is consistent within its error with the young disk. 19b-2-01387 is an outlier to the young disk criterion. Instead, Leggett (1992) define objects around the edges of the young disk ellipse as members of the young-old disk population, which has a sub-solar metallicity ($-0.5 < [m/H] < 0.0$). 19e-3-08413 exceeds the allowed W range for the young disk, despite overlap in the UV plane. Leggett (1992) assign these objects also to the young-old disk group. This suggest that two of our MEBs could be metal-poor but our spectral index measurements in Section 3.5 are not accurate enough to confirm this. We would require, for example, higher resolution, J-band spectra to assess the metallicities in detail (Önehag et al. 2011). Comparisons with space motions of solar neighbourhood moving groups do not reveal any obvious associations (Soderblom & Mayor 1993).

3.9 Discussion

3.9.1 The mass-radius diagram

Figure 3.10 shows the positions of our MEBs in the mass-radius plane and compares them to literature mass-radius measurements derived from EBs with two M-dwarfs, EBs with an M-dwarf secondary but hotter primary, eclipsing M-dwarf - white dwarf systems, and inactive single stars measured by interferometry. We only show values with reported mass and radius errors comparable to or better than our own errors. The solid line marks the 5 Gyr, solar metallicity isochrone from the Baraffe et al. (1998) models (solid line), with a convective mixing length equal to the scale height ($L_{mix} = H_P$), while the dash-dot line shows the corresponding 1 Gyr isochrone.

It is clear that some MEBs, both in the WTS and in the literature, have an excess in radius above the model predictions, and although there is no evidence to say that all MEBs disagree with the models, the scatter in radius at a given mass is clear, indicating a residual dependency on other parameters. Knigge et al. (2011) measured the average fractional radius excess below $0.7M_{\odot}$, but based on the findings of Chabrier et al. (2007) and Morales et al. (2010), split the sample at the fully-convective boundary to investigate the effect of inhibited convection. The dashed line in Figure 3.10 marks the average radius inflation they found with respect to the 5 Gyr isochrone for the fully-convective mass region below $0.35M_{\odot}$ and in the partially-convective region above (7.9% for $> 0.35M_{\odot}$, but only by 4.5% for $> 0.35M_{\odot}$). The WTS MEBs sit systematically above the 5 Gyr isochrone but appear to have good agreement with the average radius inflation for their mass range. It is interesting to note that we find similar radius excesses to the literature despite using infrared light curves. At these wavelengths, we crudely expect lower contamination of the light curves by sinusoidal star spots signals and less loss of circular symmetry, on account of the smaller difference between the spectral energy distributions of the star and the spots in the J-band. If one could eliminate the $\sim 3\%$ systematic errors in MEB radii caused by polar star spots (Morales et al. 2010) by using infrared data, yet still see similar excess, this would be evidence for a larger effect from magnetic fields (or another hidden parameter) than currently thought. Unfortunately, the errors on our radii do not allow for a robust claim of this nature, but it is an interesting avenue for the field.

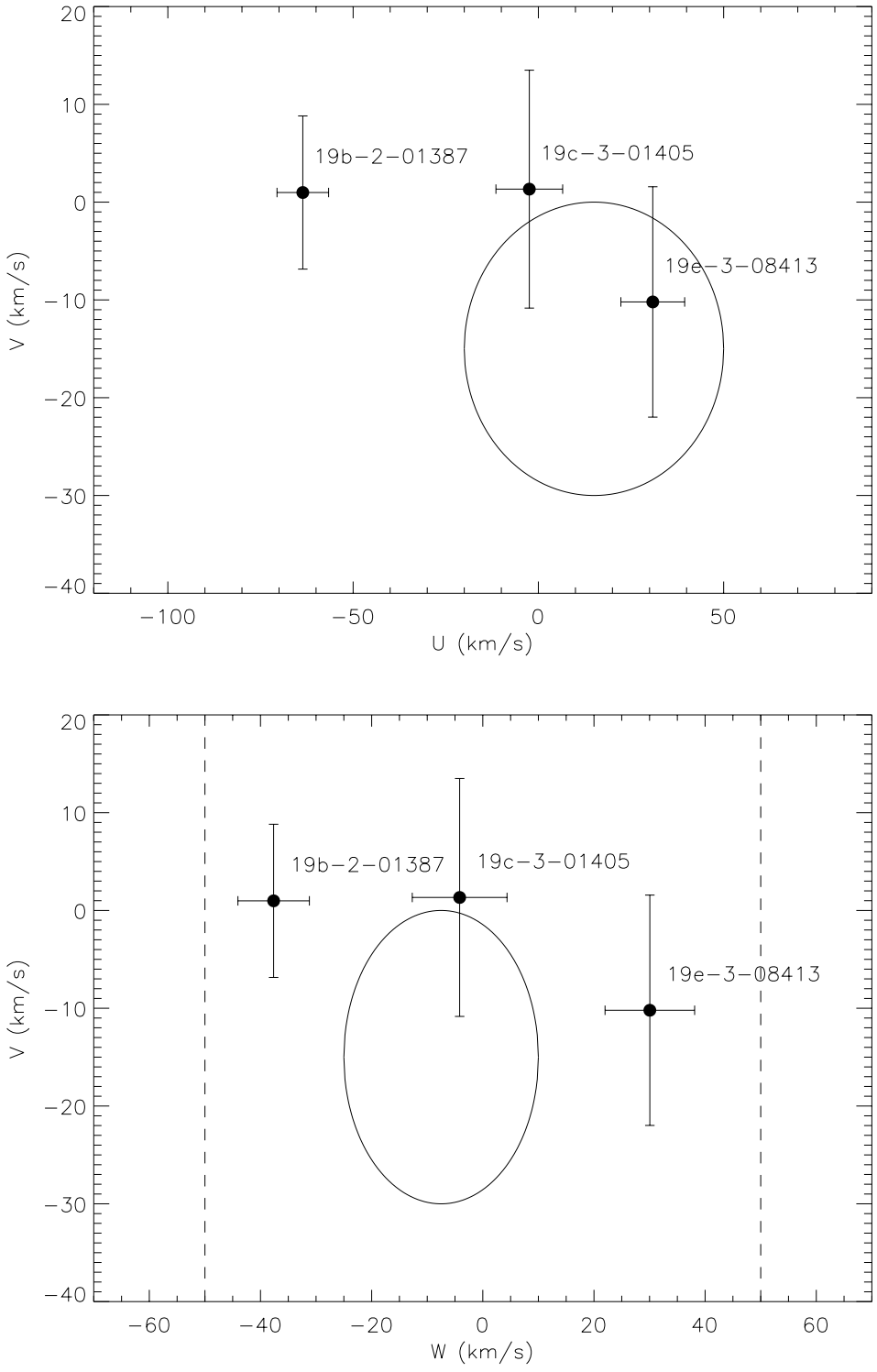

Figure 3.9 — The UVW space motions with respect to the Sun for our MEBs. The errors have been propagated according to Johnson & Soderblom (1987). The solid ellipses are the error ellipses for the young disk defined by Leggett (1992). The dashed vertical lines in the lower plot mark the W boundary within which the young-old disk population is contained (Leggett 1992).

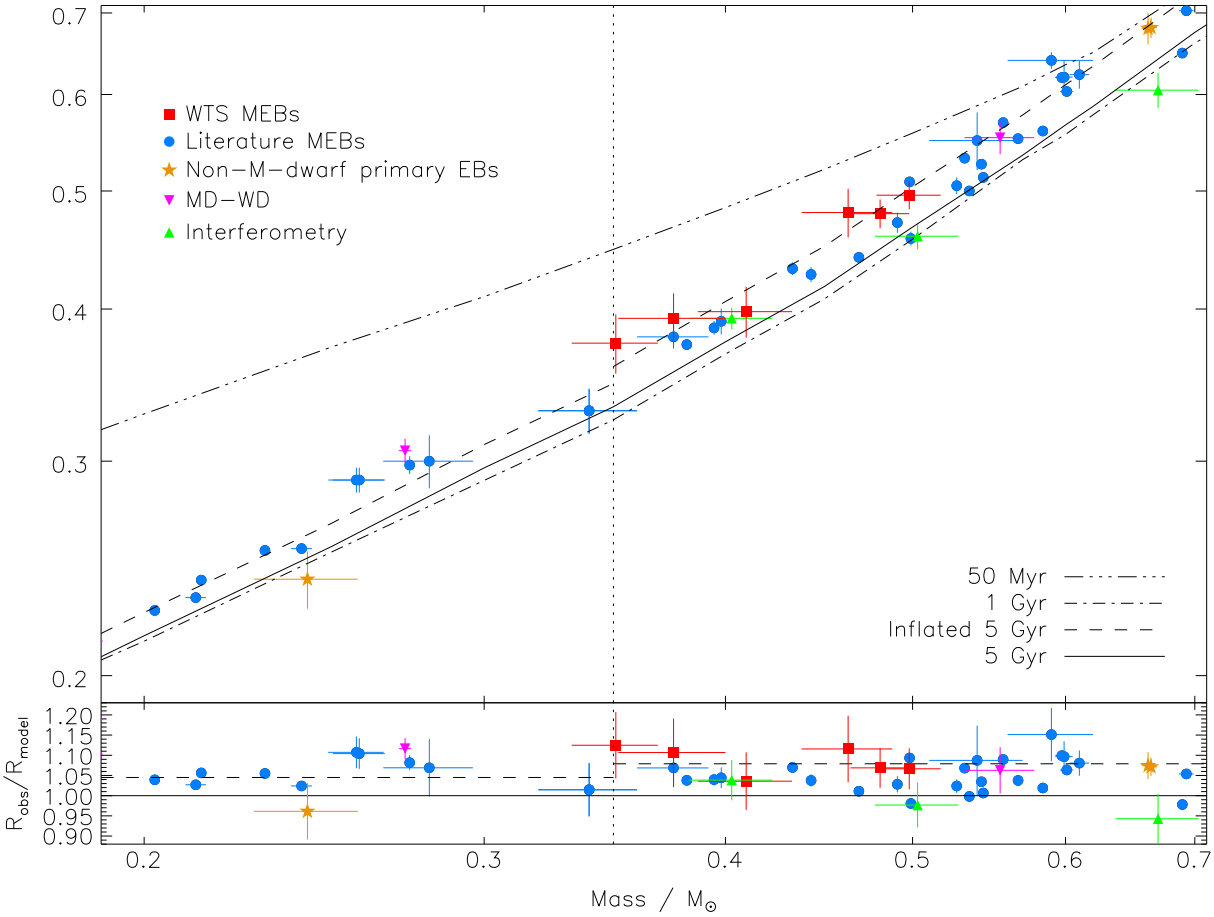

Figure 3.10 — The mass-radius diagram for low-mass stars. The filled circles show literature MEB values with reported mass errors $< 6\%$ and radius errors $< 6.5\%$. Also shown are literature values for i) the low-mass secondaries of eclipsing binaries with primary masses $> 0.6 M_{\odot}$, ii) M-dwarfs found in M-dwarf - white dwarf eclipsing binaries (MD-WD), and iii) radius measurements of single M-dwarfs from interferometric data. The red squares mark the new WTS MEBs. The diagonal lines show model isochrones from the Baraffe et al. (1998) models ($[m/H] = 0, Y = 0.275$ and $L_{mix} = H_P$), while the vertical dotted line marks the onset of fully-convective envelopes (Chabrier & Baraffe 1997). The dashed line shows the 5 Gyr isochrone plus the average radius excess found by Knigge et al. (2011), assuming a discontinuity at the fully-convective transition. Above $0.35 M_{\odot}$, the model is inflated by 7.9%, but below it is only inflated by 4.5%. The bottom panel shows the radius anomaly, $R_{\rm obs}/R_{\rm model}$ computed using the 5 Gyr isochrone and again the dashed line shows the corresponding average radius excess found byKni11. The literature data used in these plots are given in Table 3.16.

The components of our new MEBs do not seem to converge towards the standard 5 Gyr isochrone as they approach the fully-convective region. In fact, our lowest mass star, which has a mass error bar that straddles the fully-convective boundary, is the most inflated of the six components we have measured. The lower panel of Figure 3.10 illustrates this inflation more clearly by showing the radius anomaly $R_{\rm obs}/R_{\rm model}$ as a function of mass, as computed with the standard 5 Gyr isochrone. The errors on the radius anomaly include the observed error on the radius and the observed error on the mass (which propagates into the value of $R_{\rm model}$), added in quadrature. The spread in radii at a given mass is clearer here, and we discuss why stars of the same mass could be inflated by different amounts in Section 3.9.3 by considering their rotational velocities.

A comparison of the measured radii of all known MEBs to the model isochrones shown in Figure 3.10 might lead one to invoke young ages for most of the systems, because stars with $M_\star \lesssim 0.7{\rm M}_\odot$ are still contracting onto the pre-main sequence at an age $\lesssim 200$ Myr and therefore have larger radii. While young stars exist in the solar neighbourhood (as shown by e.g. Jeffries & Jewell (1993) who found an upper limit of 10-15 young stars within 25pc), it is highly unlikely that all of the known MEBs are young. Indeed, the derived surface gravities for our MEBs are consistent with older main-sequence stars. We see emission of Hα in all three systems, which can be an indicator of youth, but close binary systems are known to exhibit significantly more activity than wide binaries or single stars of the same spectral type (see e.g. Shkolnik et al. 2010). We therefore do not have independent evidence to strongly associate the inflated radii of our MEBs with young ages.

3.9.2 The mass-$T_{\rm eff}$ diagram

As discussed in Section 3.1, there is some evidence for a radius-metallicity correlation (Berger et al. 2006; López-Morales 2007) amongst M-dwarfs. Model values for effective temperatures depend on model bolometric luminosities, which are a function of metallicity. Metal-poor stars are less opaque so model luminosities and effective temperatures increase while the model radii shrink by a small amount (Baraffe et al. 1998). Figure 3.11 shows our MEBs in the mass-$T_{\rm eff}$ plane plus the same literature systems from Figure 3.10 where effective temperatures are available. The two lines show the standard 5 Gyr isochrone of the Baraffe et al. (1998) models for solar metallicity stars (solid line) and for metal-poor stars (dot-dash line).

The large errors in the mass-$T_{\rm eff}$ plane for M-dwarfs mean that it is not well-constrained. Section 3.5 has already highlighted some of difficulties in constraining effective temperatures and metallicities for M-dwarfs, but one should also note that effective temperatures reported in the literature are determined using a variety of different methods, e.g. broad-band colour indices, spectral indices, or model atmosphere fitting using several competing radiative transfer codes. It also involves a number of different spectral type - $T_{\rm eff}$ relations, and as Reyle et al. (2011) have demonstrated, these can differ by up to 500 K for a given M-dwarf subclass.

While the intrinsic scatter in the effective temperatures at a given mass may be caused by metallicity effects, the overall trend is that models predict temperatures that are too hot compared to observed values, especially below $0.45{\rm M}_\odot$. Our new MEBs, which we determined to have metallicities consistent with the Sun, also conform to this trend. Furthermore, several studies of the inflated CM Dra system have found it to be metal-poor (Viti et al. 1997, 2002), whereas models would suggest it was metal-rich for its mass, based on its cooler temperature

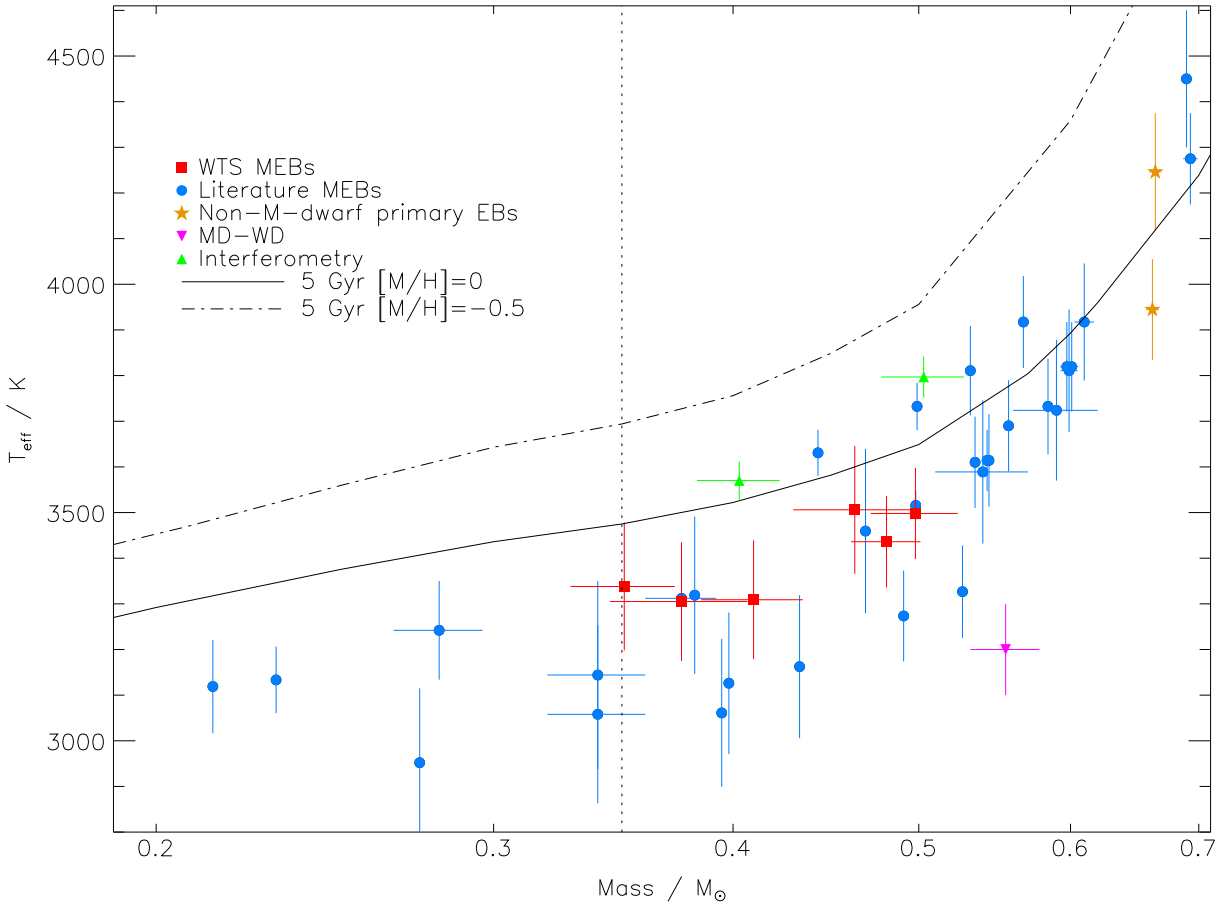

Figure 3.11 — The mass-$T_{\rm eff}$ diagram for low mass stars. Two different metallicity isochrones from the Baraffe et al. (1998) 1 Gyr models are over-plotted to show the effect of decreasing metallicity. The vertical dotted line marks the fully-convective boundary (Chabrier & Baraffe 1997). The data used in this plot are given in Table 3.16.

and larger radius (see Table 3.16 for data). In this case, the very precisely measured inflated radius of CM Dra cannot be explained by a high metallicity effect. In fact, the tentative association of two of our new MEBs with the slightly metal-poor young-old disk population defined by Leggett (1992), would also make it difficult to explain their inflated radii using the metallicity argument.

The scatter in the mass-$T_{\rm eff}$ plane can also arise from spot coverage due to the fact that very spotty stars have cooler effective temperatures at a given mass, and consequently larger radii for a fixed luminosity. Large spot coverage fractions are associated with high magnetic activity, which is induced by fast rotational velocities. Table 3.11 gives the synchronous rotational velocities of the stars in our MEBs along with their theoretical timescales for tidal circularisation and synchronisation. Among our new systems, 19c-3-01405 contains the slowest rotating stars ($\sim$ 4 km/s) on account of its longer orbital period, and its components have stellar radii that are the most consistent with the standard 5 Gyr model. The other faster rotating stars in our MEBs have radii that deviate from the model by more than 1σ. We discuss this tentative trend between radius inflation and rotational velocity (i.e. orbital period, assuming the systems are tidally-locked) in the next section.

Period	$\bar{\mu}$	$\pm\frac{\sigma}{\sqrt{N}}$	σ
All	103.7%	0.5%	3.3%
$P \leq 1.0$	106.2%	0.9%	4.0%
$P > 1.0$	102.6%	0.4%	2.4%

Table 3.12 — A statistical analysis of the mean radius inflation for different period ranges. σ is the weighted sample standard deviation.

3.9.3 A mass-radius-period relationship?

In a recent paper, Kraus et al. (2011) presented six new MEBs with masses between $0.38-0.59\mathrm{M}_{\odot}$ and short orbital periods spanning $0.6-1.7$ days. Their measurements combined with existing literature revealed that the mean radii of stars in systems with orbital periods less than 1 were different at the 2.6σ level to those at longer periods. Those with orbital periods < 1 day were systematically larger than the predicted radii by $4.8 \pm 1\%$, whereas for periods > 1.5 days the deviation from the Baraffe et al. (1998) models are much smaller ($1.7 \pm 0.7\%$). The implication is that a very short orbital period, i.e. very high level of magnetic activity, leads to greater radius inflation, and one then expects the level of radius inflation to decrease at longer periods. Figure 3.12 shows the radius anomaly (R_{obs}/R_{model}) as a function of period for our new MEBs plus literature values whose reported errors are compatible with our own measurements ($\sigma_{M_{\rm obs}} < 6\%$ and $\sigma_{R_{\rm obs}} < 6.5\%$). We used the 5 Gyr, solar metallicity isochrone from the Baraffe et al. (1998) models, with $L_{\rm mix} = H_{\rm P}$, to derive the radius anomalies. The models were linearly interpolated onto a finer grid with intervals of $0.0001\mathrm{M}_{\odot}$, and the model photospheric radii were calculated using $R_{\rm model} = \sqrt{L_{\rm model}/4\pi\sigma T^4_{\rm eff,model}}$.

Despite the small sample, we have performed an error weighted statistical analysis of the period distribution, including our new measurements, to compare to the unweighted analysis presented in Kraus et al. (2011). Table 3.12 reports the weighted mean ($\bar{\mu}$) and weighted sample standard deviation (σ) of the radius anomaly for three different period ranges: i) all periods, ii) periods ≤ 1 day and, iii) periods > 1 day. The boundary between the 'short' and 'long' period samples was chosen initially to match the analysis by Kraus et al. (2011). A T-test using the weighted mean and variances of the short and long period samples shows that their mean radii are distinct populations at a 4.0σ significance, in support of Kraus et al.'s findings. However, the significance level is strongly dependent on the chosen period boundary, and is skewed by the cluster of very precisely measured values near 1.5 days. For example, a peak significance of 4.8σ is found when dividing the sample at 1.5 days, but sharply drops to $\sim 1\sigma$ for periods of 1.7 days or longer. At short periods, it rises gradually towards the peak from 1σ at 0.3 days.

Instead, we have attempted to find a very basic mathematical description for any correlation between radius inflation and orbital period, but we appreciate our efforts are hampered by small number statistics. We fitted the distribution of the radius anomaly as a function of period, using first a linear model and then as an exponentially decaying function. We used the IDL routine MPFITFUN to determine an error weighted best-fit and the 1σ errors of the model parameters. The results are reported in Table 3.13 and the best-fit models are over-plotted in Figure 3.12, but neither model is a good fit (although the exponential fairs moderately better). While there is marginal evidence for greater inflation in the shortest period systems, we find that the ex-

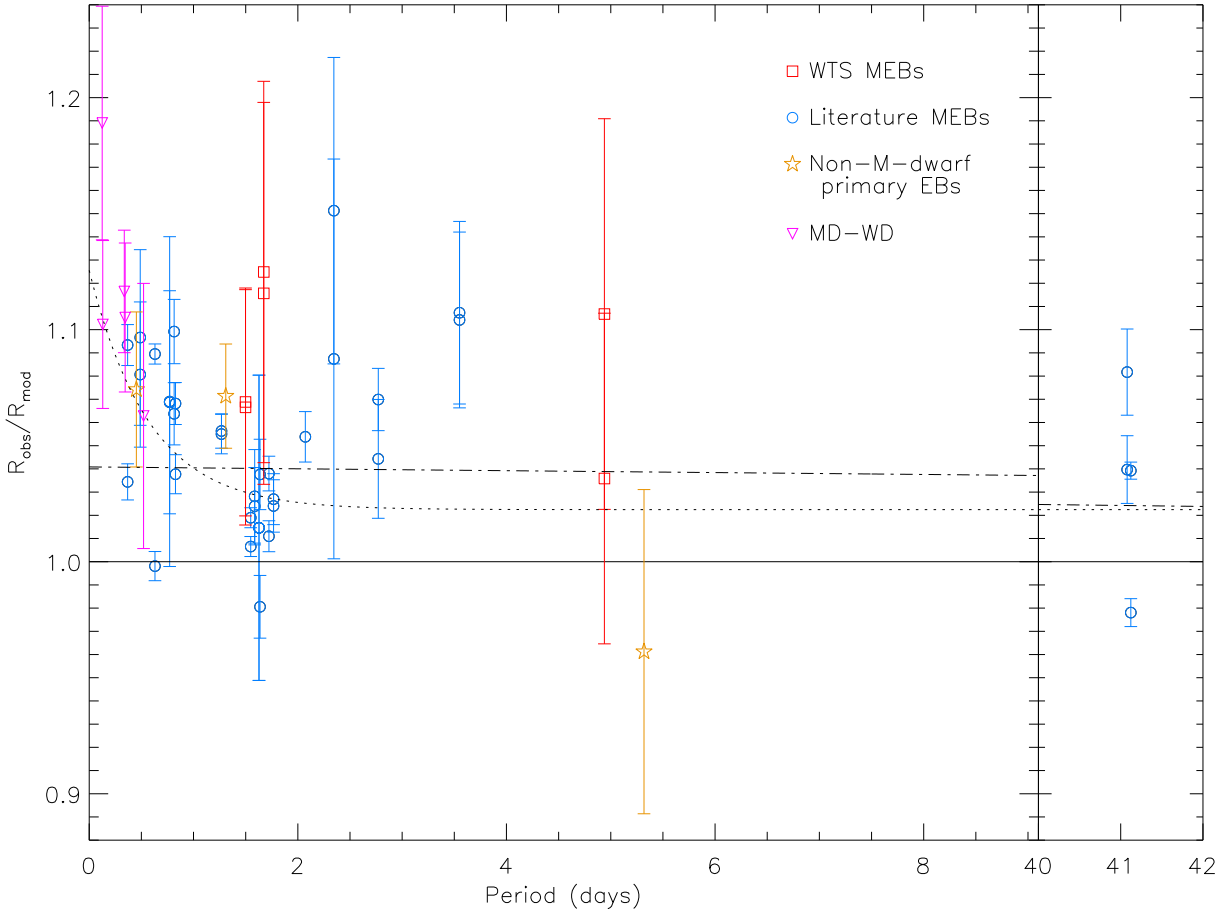

Figure 3.12 — The radius anomaly as a function of orbital period using the 5 Gyr solar-metallicity isochrone from the Baraffe et al. (1998) models. Our new MEBs are shown by the red open squares. Literature radius anomalies with radius errors $< 6.5\%$ are also plotted. The errors are a quadrature sum of the measured radius error plus a propagated error from the observed mass which determines the model radius. The dashed and dotted lines show the best-fit from a straight-line and exponentially decaying model to the data, respectively. The coefficients and goodness of fit for these fits are given in Table 3.13. The data used in this plot are given in Table 3.16.

pected convergence towards theoretical radius values for longer period, less active systems is not significantly supported by the available observation data.

There are two pertinent observations worth addressing, namely the low-mass eclipsing binaries LSPM J1112+7626 and Kepler-16 (Irwin et al. 2011; Doyle et al. 2011; Bender et al. 2012), which were announced after the Kraus et al. (2011) study. These systems significantly extended the observed orbital period range, with almost identical 41-day orbital periods, and both containing one fully-convective component ($M_\star \sim 0.35 M_\odot$, Chabrier & Baraffe 1997) and one partially convective component (see Table 3.16). The radius inflation differs significantly between these two systems, as shown on the right-hand side of Figure 3.12. While the more massive, partially-convective component of Kepler-16 is well-described by the 1 Gyr model isochrone Baraffe et al. (1998) (see Figure 3.10), the other three stars suffer significant radius inflation, with no obvious correlation between the amount of inflation and the masses, even though one of them is a partially-convective star. This residual inflation, particularly for the

Model ($R_{\rm obs}/R_{\rm mod} =$)	a_0	a_1	a_2	χ^2	DOF	χ^2_ν
$a_0 + a_1 P$	1.0408 ± 0.0017	-0.000406 ± 0.000086	–	514.5	49	10.5
$a_0 + a_1 e^{a_2 P}$	1.0224 ± 0.0027	0.103 ± 0.017	-1.75 ± 0.34	405.0	48	8.4

Table 3.13 — Results from an error weighted modelling of the radius anomaly as a function of period. a_i are the coefficients of the models and P is the orbital period in days. Neither of these simple models provide a statistically good fit, indicating a more complex relationship between the radius anomaly and orbital period.

fully-convective stars at long periods, may pose a challenge to the magnetic activity hypothesis as the sole reason for discrepancies between models and observations, especially given the extremely high-quality measurements of Kepler-16. However, one should note that other studies have suggested that the presence of a strong magnetic field can alter the interior structure of a low-mass star, such that is pushes the fully-convective mass limit for very active stars to lower values (Mullan & MacDonald 2001; Chabrier et al. 2007), so these stars may still suffer from a significant inhibition of convective flow.

The radius anomaly raises concern over the usefulness of the known MEBs in calibrating models for the evolution of singular M-dwarf stars that are the favoured targets of planet-hunting surveys searching for habitable worlds. Kraus et al. (2011) argue that the high-activity levels in very close MEBs make them poor representatives of typical single low-mass stars and that the observed radius discrepancies should not be taken as an indictment of stellar evolution models. However, we have seen that radius inflation remains in MEBs systems with low magnetic activity and furthermore, the inflated components of LSPM J1112+7626 do not exhibit Hα emission that is typically associated with the high activity levels in MEBs with inflated radii. West et al. (2011) used Hα emission as an activity indicator to determine that the fraction of single, active, early M-dwarfs is small ($< 5\%$), but increases to $40-80\%$ for M4-M9 dwarfs. Yet, it may be that the amount of activity needed to inflate radii to the measured values in MEBs is small and therefore below the level where observable signatures appear in Hα emission. This would then question the reliability of Hα emission as an activity indicator, meaning the fraction of 'active', single M-dwarfs may be even higher than the West et al. (2011) study. Given that these very small stars are a ripe hunting-ground for Earth-size planets, we must be able to constrain stellar evolution models in the presence of magnetic activity if we are to correctly characterise planetary companions. We note that even the very precisely-calibrated higher-mass stellar evolution models (Andersen 1991; Torres et al. 2010) do not reproduce the radii of active stars accurately (see Morales et al. (2009) who found $4-8\%$ inflation in a G7+K7 binary with a 1.3 day orbit).

In order to establish a stringent constraint on the relationship between mass, period and radius, we need further measurements of systems that i) include 'active' and 'non-active' stars that span the fully-convective and partially-convective mass regimes, and ii) a better sampled range of orbital periods beyond 5 days to explore systems that are not synchronised. We may ultimately find that activity does not account for the full extent of the radius anomaly, and as suggested by Irwin et al. (2011), perhaps the equation of state for low-mass stars can still be improved. On the other hand, perhaps the importance of tidal effects between M-dwarfs in binaries with wider separations has been underestimated, as it has been shown that the orbital evolution of M-dwarf binary systems is not well-described by current models (Nefs et al. 2012).

3.10 Conclusions

In this paper, we have presented a catalogue of 16 new low-mass, detached eclipsing binaries that were discovered in the WFCAM Transit Survey. This is the first time dynamical measurements of M-dwarf EBs have been detected and measured primarily with infrared data. The survey light curves are of high quality, with a per epoch photometric precision of $3-5$ mmag for the brightest targets ($J \sim 13$ mag), and a median RMS of $\lesssim 1\%$ for $J \lesssim 16$ mag. We have reported the characterisation of three of these new systems using follow-up spectroscopy from ground-based $2-4$ m class telescopes. The three systems ($i = 16.7-17.6$ mag) have orbital periods in the range $1.5-4.9$ days, and span masses $0.35-0.50\mathrm{M}_{\odot}$ and radii $0.38-0.50\mathrm{R}_{\odot}$, with uncertainties of $\sim 3.5-6.4\%$ in mass and $\sim 2.7-5.5\%$ in radius. Two of the systems may be associated with the young-old disk population as defined by Leggett (1992) but our metallicity estimates from low-resolution spectra do not confirm a non-solar metallicity.

The radii of some of the stars in these new systems are significantly inflated above model predictions ($\sim 3-12\%$). We analysed their radius anomalies along with literature data as a function of the orbital period (a proxy for activity). Our error-weighted statistical analysis revealed marginal evidence for greater radius inflation in very short orbital periods < 1 day, but neither a linear nor exponentially decay model produced a significant fit to the data. As a result, we found no statistically significant evidence for a correlation between the radius anomaly and orbital period, but we are limited by the small sample of precise mass and radius measurements for low-mass stars. However, it is clear that radius inflation exists even at longer orbital periods in systems with low (or undetectable) levels of magnetic activity. A robust calibration of the effect of magnetic fields on the radii of M-dwarfs is therefore a key component in our understanding of these stars. Furthermore, it is a limiting factor in characterising the planetary companions of M-dwarfs, which are arguably our best targets in the search for habitable worlds and the study of other Earth-like atmospheres.

More measurements of the masses, radii and orbital periods of M-dwarf eclipsing binaries, spanning both the fully convective regime and partially convective mass regime, for active and non-active stars, across a range of periods extending beyond 5 days, are necessary to provide stringent observational constraints on the role of activity in the evolution of single low-mass stars. However, the influence of spots on the accuracy to which we can determine the radii from light curves will continue to impede these efforts, even in the most careful of cases (see e.g. Morales et al. 2010; Irwin et al. 2011).

This work has studied only one third of the M-dwarfs in the WFCAM Transit Survey. Observations are on-going and we expect our catalogue of M-dwarf eclipsing binaries to increase. This forms part of the legacy of the WTS and will provide the low-mass star community with high-quality MEB light curves. Furthermore, the longer the WTS runs, the more sensitive we become to valuable long-period, low-mass eclipsing binaries. These contributions plus other M-dwarf surveys, such as MEarth and PTF/M-dwarfs, will ultimately provide the observational calibration needed to anchor the theory of low-mass stellar evolution.

Acknowledgements

We would like to thank I. Baraffe for providing the model magnitudes for our SED fitting in the appropriate filters, and S. Aigrain for the use of the OCCFIT transit detection algorithm. This work was greatly improved by several discussions with J. Irwin, as well as J. Southworth, K. Stassun and R. Jeffries. We thank the referee for their insightful comments which have improved this work and we also thank C. del Burgo for his comments on the original manuscript. JLB acknowledges the support of an STFC PhD studentship during part of this research. We thank the members of the WTS consortium and acknowledge the support of the RoPACS network. GK, BS, PC, NG, and HS are supported by RoPACS, while JLB, BN, SH, IS, DP, DB, RS, EM and YP have received support from RoPACS during this research, a Marie Curie Initial Training Network funded by the European CommissionâĂŹs Seventh Framework Programme. NL is supported by the national program AYA2010-19136 funded by the Spanish ministry of science and innovation. Finally, we extend our thanks to the fantastic team of TOs and support staff at UKIRT, and all those observers who clicked on U/CMP/2.

The United Kingdom Infrared Telescope is operated by the Joint Astronomy Centre on behalf of the Science and Technology Facilities Council of the U.K. This article is based on observations made with the INT, WHT operated on the island of La Palma by the ING in the Spanish Observatorio del Roque de los Muchachos, and with the IAC80 on the island of Tenerife operated by the IAC in the Spanish Observatorio del Teide. This research uses products from SDSS DR7. Funding for the SDSS and SDSS-II has been provided by the Alfred P. Sloan Foundation, the Participating Institutions, the National Science Foundation, the U.S. Department of Energy, the National Aeronautics and Space Administration, the Japanese Monbukagakusho, the Max Planck Society, and the Higher Education Funding Council for England. The SDSS Web Site is http://www.sdss.org/. This publication makes use of data products from the Two Micron All Sky Survey, which is a joint project of the University of Massachusetts and the Infrared Processing and Analysis Center/California Institute of Technology, funded by the National Aeronautics and Space Administration and the National Science Foundation. This work also makes use of NASAâĂŹs Astrophysics Data System (ADS) bibliographic services, and the SIMBAD database, operated at CDS, Strasbourg, France. IRAF is distributed by the National Optical Astronomy Observatory, which is operated by the Association of Universities for Research in Astronomy (AURA) under cooperative agreement with the National Science Foundation.

Appendix

In Table 3.14, we present the periods, epochs, effective temperatures, *J*-band and *i*-band magnitudes of the 13 remaining 19hr detached, well-sampled M-dwarf eclipsing binaries found with this study ($J \leq 16$ mag). The temperatures are based on the SED fitting described in Section 3.4.1 and may be under-estimated. The periods and epochs are based only on least-square fitting which under-estimates the errors. These results are accurate to ~ 30 minutes and we recommend to anyone planning to observe these objects in a time critical manner that they check these values themselves with the light curve data provided with this paper. Note that 19g-4-02069 is the subject of a near future publication (Nefs et al. *in prep.*) using RVs follow-up already obtained with GNIRS/GEMINI. The phase-folded light curves are shown in Figures 3.13. and 3.14, and the light curve data are provide in Table 3.15.

Name	RA (deg)	Dec (deg)	$N_{\rm epochs}$	RMS (mag)	P (days)	T_0 (HJD)	J (Vega) (mag)	i (Vega) (mag)	$T_{\rm eff,SED}$ (K)
19a-1-02980	292.71276	36.312725	893	5.8	2.103525	2454318.65422	14.861	16.166	3946
							±0.004	±0.004	±100
19c-3-08647	294.30659	36.815037	893	15.0	0.867466	2454318.50614	14.812	16.171	3883
							±0.004	±0.004	±100
19c-4-11480	293.81149	36.902880	893	20.4	0.681810	2454317.89071	15.850	17.208	3946
							±0.006	±0.007	±100
19d-2-07671	294.58622	36.386467	891	48.9	0.614540	2454317.99692	15.971	17.101	4209
							±0.007	±0.007	±100
19d-2-09173	294.50246	36.365239	891	22.4	3.345469	2454320.15668	15.185	16.343	4209
							±0.005	±0.005	±100
19e-2-02883	293.32813	36.241312	898	10.6	0.810219	2454317.90290	15.976	17.272	3946
							±0.007	±0.007	±100
19f-1-07389	292.89403	36.143865	904	18.3	0.269868	2454317.97411	15.504	16.575	4209
							±0.005	±0.005	±100
19f-4-05194	292.81253	36.590539	904	35.0	0.589530	2454318.10730	16.013	17.070	4209
							±0.007	±0.006	±100
19g-1-13215	293.63655	36.249009	898	10.2	2.843515	2454318.34495	15.985	17.589	3374
							±0.007	±0.008	±100
19g-2-08064	294.16931	36.162723	898	14.8	1.720410	2454317.94781	14.466	15.596	4209
							±0.003	±0.004	±100
19g-4-02069	293.76480	36.521247	898	11.2	2.441759	2454321.78532	14.843	16.911	3054
							±0.004	±0.006	±100
19h-2-00357	294.66466	36.272874	885	8.3	7.004082	2454320.79766	15.531	16.808	3946
							±0.005	±0.006	±100
19h-2-01090	294.62103	36.262345	886	11.5	5.285051	2454322.78131	15.681	16.843	4209
							±0.006	±0.006	±100

Table 3.14 — The first release of the WTS M-dwarf Eclipsing Binary Catalogue detailing the remaining MEBs in the WTS 19hr field with $J \leq 16$ mag that are not characterised in this paper. Note that 19g-4-02069 is the subject for a near future publication by Nefs et al. (*in prep.*) using RV follow-up from GNIRS/GEMINI. Please see appendix text for caveats on the quoted ephemerides.

Name	HJD	$J_{\rm WTS}$ (mag)	$\sigma_{J_{\rm WTS}}$ (mag)
19a-1-02980	2454317.82863842	14.846761	0.004826
19a-1-02980	2454317.84010834	14.844511	0.004894
...	...	...	...

Table 3.15 — The WTS J-band light curves for the remainder of the WTS MEB catalogue given in Table 3.14 Magnitudes are given in the WFCAM system. Hodgkin et al. (2009) provide conversions for other systems. The errors, σ_J, are estimated using a standard noise model, including contributions from Poisson noise in the stellar counts, sky noise, readout noise and errors in the sky background estimation. (This table is published in full in the online journal and is shown partially here for guidance regarding its form and content.)

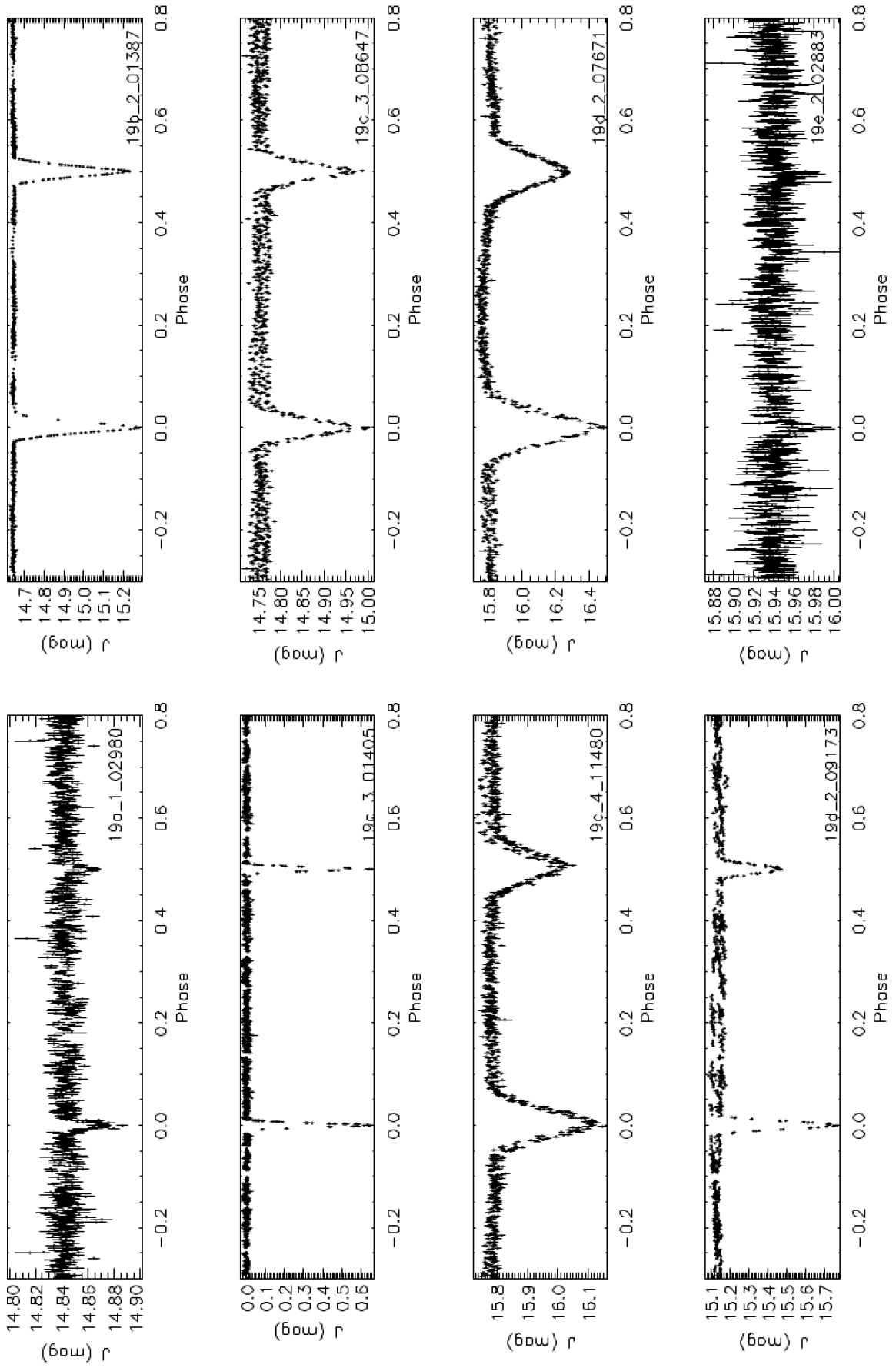

Figure 3.13 — Phase-folded light curves of the MEBs discovered in the WTS 19hr field with $J \leq 16$ mag...

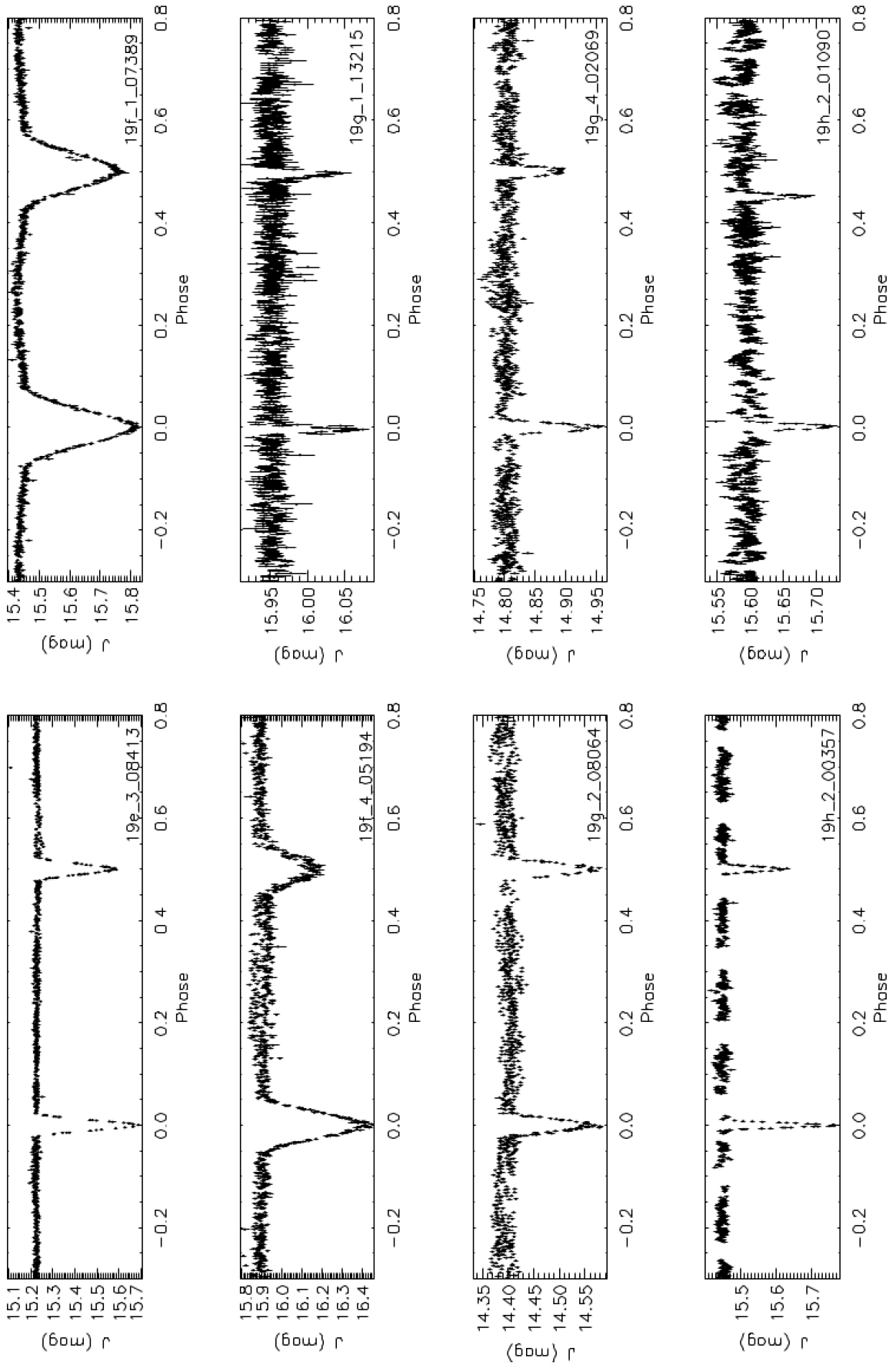

Figure 3.14 — cont... Phase-folded light curves of the MEBs discovered in the WTS 19hr field with $J \leq 16$ mag.

Table 3.16 contains the literature data used to create Figures 3.10, 3.11 and 3.12. The literature data was selected with the following filters: mass errors $< 6.4\%$ and radius errors $< 5.5\%$ (comparable to or better than the errors we presented for the three characterised MEBs in this paper), and in the range $0.19 \leq M_\star \leq 0.71$ and $0.19 \leq R_\star \leq 0.71$.

Table 3.16 — Literature values for systems used in Figures 3.10, 3.11 and 3.12

Name	Period (days)	Mass ($M_\odot$)	σ_M ($M_\odot$)	Radius ($R_\odot$)	σ_R ($R_\odot$)	T_{eff} (K)	$\sigma_{T_{eff}}$ (K)	Ref
MEBs								
NSVS01031772A	0.368	0.5428	0.0028	0.5260	0.0028	3614.1	67.2	(1)
NSVS01031772B	0.368	0.4982	0.0025	0.5087	0.0031	3515.6	32.5	(1)
GUBooA	0.489	0.6100	0.0071	0.6230	0.0163	3917.4	128.3	(1)
GUBooB	0.489	0.5990	0.0061	0.6200	0.0203	3810.7	133.9	(1)
MG1-1819499A	0.6303135	0.557	0.001	0.569	0.002	3690.0	100.0	(2)
MG1-1819499B	0.6303135	0.535	0.001	0.500	0.003	3610.0	100.0	(2)
GJ3236A	0.77126	0.376	0.016	0.3795	0.0084	3312.0	110.0	(3)
GJ3236B	0.77126	0.281	0.015	0.300	0.015	3242.0	108.0	(3)
YYGemA	0.814	0.5974	0.0047	0.6196	0.0057	3819.4	98.0	(1)
YYGemB	0.814	0.6009	0.0047	0.6035	0.0057	3819.4	98.0	(1)
MG1-116309A	0.8271425	0.567	0.002	0.552	0.004	3917.4	100.5	(2)
MG1-116309B	0.8271425	0.532	0.002	0.532	0.004	3810.7	97.8	(2)
CMDraA	1.268	0.2310	0.0009	0.2534	0.0019	3133.3	73.0	(1)
CMDraB	1.268	0.2141	0.0009	0.2396	0.0015	3118.9	102.2	(1)
MG1-506664A	1.5484492	0.584	0.002	0.560	0.001	3732.5	104.6	(2)
MG1-506664B	1.5484492	0.544	0.002	0.513	0.001	3614.1	101.3	(2)
MG1-78457A	1.5862046	0.5270	0.0019	0.505	0.008	3326.6	101.1	(2)
MG1-78457B	1.5862046	0.491	0.002	0.471	0.009	3273.4	99.5	(2)
LP133-373A	1.6279866	0.34	0.02	0.330	0.014	3144.0	206.0	(4)
LP133-373B	1.6279866	0.34	0.02	0.330	0.014	3058.0	195.0	(4)
MG1-646680A	1.6375302	0.499	0.002	0.457	0.006	3732.5	51.9	(2)
MG1-646680B	1.6375302	0.443	0.002	0.427	0.006	3630.8	50.5	(2)
MG1-2056316A	1.7228208	0.4690	0.0021	0.441	0.002	3459.4	179.8	(2)
MG1-2056316B	1.7228208	0.382	0.002	0.374	0.002	3318.9	172.5	(2)
KOI126B	1.76713	0.2413	0.0030	0.2543	0.0014	–	–	(5)
KOI126C	1.76713	0.2127	0.0026	0.2318	0.0013	–	–	(5)
HIP96515Aa	2.3456	0.59	0.03	0.64	0.01	3724.0	154.0	(6)
HIP96515Ab	2.3456	0.54	0.03	0.55	0.03	3589.0	157.0	(6)
CUCncA	2.771	0.4333	0.0017	0.4317	0.0052	3162.3	156.7	(1)
CUCncB	2.771	0.3980	0.0014	0.3908	0.0095	3126.1	154.9	(1)
1RXSJ154727A	3.5500184	0.2576	0.0085	0.2895	0.0068	–	–	(7)
1RXSJ154727B	3.5500184	0.2585	0.0080	0.2895	0.0068	–	–	(7)
LSPMJ1112A	41.03236	0.3946	0.0023	0.3860	0.005	3061.0	162.0	(8)
LSPMJ1112B	41.03236	0.2745	0.0012	0.2978	0.005	2952.0	163.0	(8)

Continued on next page

Table 3.16 – continued from previous page

Name	Period	Mass	σ_M	Radius	σ_R	$T_{\rm eff}$	$\sigma_{T_{\rm eff}}$	Ref
Kepler16A	41.079220	0.6897	0.0035	0.6489	0.0013	4450	150	(9)
Kepler16B	41.079220	0.20255	0.00066	0.22623	0.00059	–	–	(9)
Non-M-dwarf primary EBs								
NGC-2204-S892B	0.452000	0.6621	0.0050	0.6800	0.0203	3944.6	110.5	(1)
IM-VirB	1.309000	0.6644	0.0048	0.6809	0.0131	4246.2	129.0	(1)
RXJ0239B	2.072016	0.693	0.006	0.703	0.002	4275.0	109.0	(10)
MD-WD EBs								
SDSS 1210	0.12448976	0.158	0.006	0.2135	0.003	–	–	(11)
NNSerB	0.13008017	0.111	0.004	0.149	0.002	–	–	(12)
SDSS 0123	0.33587114	0.273	0.002	0.306	0.007	–	–	(13)
GKVir	0.34433083	0.116	0.003	0.155	0.003	–	–	(13)
RXJ2130	0.5210356	0.555	0.023	0.553	0.017	3200.0	100.0	(10)
Interferometry								
GJ411	–	0.403	0.020	0.393	0.008	3570.0	42.0	(14)
GJ380	–	0.670	0.033	0.605	0.020	–	–	(14)
GJ887	–	0.503	0.025	0.459	0.011	3797.0	45.0	(15)

Table 3.16 — Literature values for systems used in Figures 3.10, 3.11 and 3.12 with mass errors $<$ 6.4% and radius errors $<$ 5.5%, in the range $0.19 \leq M_\star \leq 0.71$ and $0.19 \leq R_\star \leq 0.71$. Temperatures are given when available in the literature, but those without are not included in Figure 3.10. There are no rotation periods given for the interferometric measurements therefore these are excluded from Figure 3.12. References: (1) DEBCat and references therein (www.astro.keele.ac.uk/jkt/debcat/), (2) Kraus et al. (2011), (3) Irwin et al. (2009), (4) Vaccaro et al. (2007), (5) Carter et al. (2011), (6) Huélamo et al. (2009), (7) Hartman et al. (2011), (8) Irwin et al. (2011), (9) Doyle et al. (2011), (10) Knigge et al. (2011) and references therein, (11) Pyrzas et al. (2012), (12) Parsons et al. (2010), (13) Parsons et al. (2012), (14) Ségransan et al. (2003), (15) Demory et al. (2009).

Bibliography

Aigrain, S., Hodgkin, S., Irwin, J., et al. 2007, MNRAS, 375, 29
Aigrain, S. & Irwin, M. 2004, MNRAS, 350, 331
Allard, F., Hauschildt, P. H., Alexander, D. R., & Starrfield, S. 1997, ARA&A, 35, 137
Andersen, J. 1991, A&A Rev., 3, 91
Andersen, J., Clausen, J. V., & Nordstrom, B. 1980, in IAU Symposium, Vol. 88, Close Binary Stars: Observations and Interpretation, ed. M. J. Plavec, D. M. Popper, & R. K. Ulrich, 81–86
Bailer-Jones, C. A. L. & Lamm, M. 2003, MNRAS, 339, 477
Bakos, G., Noyes, R. W., Kovács, G., et al. 2004, PASP, 116, 266
Baraffe, I., Chabrier, G., Allard, F., & Hauschildt, P. H. 1998, A&A, 337, 403
Barrado y Navascués, D. & Martín, E. L. 2003, AJ, 126, 2997
Batalha, N. M., Borucki, W., Caldwell, D. A., et al. 2006, in Bulletin of the American Astronomical Society, Vol. 38, American Astronomical Society Meeting Abstracts, 210.08
Bender, C. F., Mahadevan, S., Deshpande, R., et al. 2012, arXiv:1205.0259
Berger, D. H., Gies, D. R., McAlister, H. A., et al. 2006, ApJ, 644, 475
Bessell, M. S., Castelli, F., & Plez, B. 1998, A&A, 333, 231
Birkby, J., Hodgkin, S., Pinfield, D., & WTS consortium. 2011, in Astronomical Society of the Pacific Conference Series, Vol. 448, Astronomical Society of the Pacific Conference Series, ed. C. Johns-Krull, M. K. Browning, & A. A. West, 803
Bonanos, A. Z. 2007, in IAU Symposium, Vol. 240, IAU Symposium, ed. W. I. Hartkopf, E. F. Guinan, & P. Harmanec, 79–87
Carter, J. A., Fabrycky, D. C., Ragozzine, D., et al. 2011, Science, 331, 562
Casali, M., Adamson, A., Alves de Oliveira, C., et al. 2007, A&A, 467, 777
Chabrier, G. & Baraffe, I. 1997, A&A, 327, 1039
Chabrier, G., Baraffe, I., Allard, F., & Hauschildt, P. H. 2005, arXiv:astro-ph/0509798
Chabrier, G., Gallardo, J., & Baraffe, I. 2007, A&A, 472, L17
Claret, A. 2000, A&A, 363, 1081
Claret, A. 2004, A&A, 428, 1001
Covey, K. R., Ivezić, Ž., Schlegel, D., et al. 2007, AJ, 134, 2398
Cruz, K. L., Reid, I. N., Liebert, J., Kirkpatrick, J. D., & Lowrance, P. J. 2003, AJ, 126, 2421
de Mooij, E. J. W., Brogi, M., de Kok, R. J., et al. 2012, A&A, 538, A46
Deeg, H. J. & Doyle, L. R. 2001, in Third Workshop on Photometry, ed. W. J. Borucki & L. E. Lasher, 85
Del Burgo, C., Deshpande, R., Martín, E. L., et al. 2011, Research, Science and Technology of Brown Dwarfs and Exoplanets: Proceedings of an International Conference held in Shangai on Occasion of a Total Eclipse of the Sun, Shangai, China, Edited by E.L. Martin; J. Ge; W. Lin; EPJ Web of Conferences, Volume 16, id.04006, 16, 4006
Demory, B., Ségransan, D., Forveille, T., et al. 2009, A&A, 505, 205
Dhital, S., West, A. A., Stassun, K. G., et al. 2011, arXiv:1112.2670
Doyle, L. R., Carter, J. A., Fabrycky, D. C., et al. 2011, Science, 333, 1602
Drimmel, R., Cabrera-Lavers, A., & López-Corredoira, M. 2003, A&A, 409, 205
Dunham, E. W., Mandushev, G. I., Taylor, B. W., & Oetiker, B. 2004, PASP, 116, 1072
Etzel, P. B. 1980, Information Bulletin on Variable Stars, 1900, 1
Girardi, L., Bertelli, G., Bressan, A., et al. 2002, A&A, 391, 195

Gizis, J. E. 1997, AJ, 113, 806
Guinan, E. F., Fitzpatrick, E. L., Dewarf, L. E., et al. 1998, ApJ, 509, L21
Gustafsson, B., Edvardsson, B., Eriksson, K., et al. 2008, A&A, 486, 951
Hartman, J. D., Bakos, G. Á., Noyes, R. W., et al. 2011, AJ, 141, 166
Henry, T. J., Ianna, P. A., Kirkpatrick, J. D., & Jahreiss, H. 1997, AJ, 114, 388
Hewett, P. C., Warren, S. J., Leggett, S. K., & Hodgkin, S. T. 2006, MNRAS, 367, 454
Hillenbrand, L. A. & White, R. J. 2004, ApJ, 604, 741
Hoaglin, D. C., Mosteller, F., & Tukey, J. W. 1983, Understanding robust and exploratory data anlysis (Wiley)
Hodgkin, S. T., Irwin, M. J., Hewett, P. C., & Warren, S. J. 2009, MNRAS, 394, 675
Huélamo, N., Vaz, L. P. R., Torres, C. A. O., et al. 2009, A&A, 503, 873
Irwin, J., Aigrain, S., Hodgkin, S., et al. 2007a, MNRAS, 380, 541
Irwin, J., Charbonneau, D., Berta, Z. K., et al. 2009, ApJ, 701, 1436
Irwin, J., Irwin, M., Aigrain, S., et al. 2007b, MNRAS, 375, 1449
Irwin, J. M., Quinn, S. N., Berta, Z. K., et al. 2011, ApJ, 742, 123
Irwin, M. & Lewis, J. 2001, New Astronomy Review, 45, 105
Irwin, M. J. 1985, MNRAS, 214, 575
Jackson, R. J., Jeffries, R. D., & Maxted, P. F. L. 2009, MNRAS, 399, L89
Jeffries, R. D. & Jewell, S. J. 1993, MNRAS, 264, 106
Johnson, D. R. H. & Soderblom, D. R. 1987, AJ, 93, 864
Jones, H. R. A., Longmore, A. J., Jameson, R. F., & Mountain, C. M. 1994, MNRAS, 267, 413
Kervella, P., Thévenin, F., Di Folco, E., & Ségransan, D. 2004, A&A, 426, 297
Kirkpatrick, J. D., Henry, T. J., & McCarthy, Jr., D. W. 1991, ApJS, 77, 417
Knigge, C., Baraffe, I., & Patterson, J. 2011, arXiv:1102.2440
Koppenhoefer, J., Afonso, C., Saglia, R. P., & Henning, T. 2009, A&A, 494, 707
Kraus, A. L., Tucker, R. A., Thompson, M. I., Craine, E. R., & Hillenbrand, L. A. 2011, ApJ, 728, 48
Law, N. M., Kraus, A. L., Street, R. R., et al. 2011, arXiv:1101.0630
Lawrence, A., Warren, S. J., Almaini, O., et al. 2007, MNRAS, 379, 1599
Leggett, S. K. 1992, ApJS, 82, 351
Lépine, S., Rich, R. M., & Shara, M. M. 2007, ApJ, 669, 1235
Lodieu, N., Dobbie, P. D., & Hambly, N. C. 2011, A&A, 527, A24
López-Morales, M. 2007, ApJ, 660, 732
López-Morales, M. & Ribas, I. 2005, ApJ, 631, 1120
Lucy, L. B. 1967, Zeitschrift fur Astrophysik, 65, 89
Mann, A. W., Gaidos, E., Lépine, S., & Hilton, E. 2012, arXiv:1202.5394
Markwardt, C. B. 2009, in Astronomical Society of the Pacific Conference Series, Vol. 411, Astronomical Data Analysis Software and Systems XVIII, ed. D. A. Bohlender, D. Durand, & P. Dowler, 251
Miller, A. A., Irwin, J., Aigrain, S., Hodgkin, S., & Hebb, L. 2008, MNRAS, 387, 349
Morales, J. C., Gallardo, J., Ribas, I., et al. 2010, ApJ, 718, 502
Morales, J. C., Ribas, I., Jordi, C., et al. 2009, ApJ, 691, 1400
Muirhead, P. S., Hamren, K., Schlawin, E., et al. 2011, arXiv:1109.1819
Mullan, D. J. & MacDonald, J. 2001, ApJ, 559, 353
Munn, J. A., Monet, D. G., Levine, S. E., et al. 2004, AJ, 127, 3034

Munn, J. A., Monet, D. G., Levine, S. E., et al. 2008, AJ, 136, 895
Nefs, S. V., Birkby, J. L., Snellen, I. A. G., et al. 2012, arXiv:1206.1200
Nelson, B. & Davis, W. D. 1972, ApJ, 174, 617
Nordstrom, B. & Johansen, K. T. 1994, A&A, 291, 777
Nutzman, P. & Charbonneau, D. 2008, PASP, 120, 317
Önehag, A., Heiter, U., Gustafsson, B., et al. 2011, arXiv:1112.0141
Parsons, S. G., Marsh, T. R., Copperwheat, C. M., et al. 2010, MNRAS, 402, 2591
Parsons, S. G., Marsh, T. R., Gänsicke, B. T., et al. 2012, MNRAS, 420, 3281
Pollacco, D. L., Skillen, I., Cameron, A. C., et al. 2006, PASP, 118, 1407
Pont, F., Zucker, S., & Queloz, D. 2006, MNRAS, 373, 231
Popper, D. M. 1984, Mitteilungen der Astronomischen Gesellschaft Hamburg, 62, 19
Popper, D. M. & Etzel, P. B. 1981, AJ, 86, 102
Press, W. H., Teukolsky, S. A., Vetterling, W. T., & Flannery, B. P. 1992, Numerical recipes in FORTRAN. The art of scientific computing (Cambridge: University Press, |c1992, 2nd ed.)
Pyrzas, S., Gänsicke, B. T., Brady, S., et al. 2012, MNRAS, 419, 817
Reid, I. N., Hawley, S. L., & Gizis, J. E. 1995, AJ, 110, 1838
Reyle, C., Rajpurohit, A. S., Schultheis, M., & Allard, F. 2011, arXiv:1102.1263
Ribas, I. 2006, Ap&SS, 304, 89
Ribas, I., Jordi, C., Vilardell, F., et al. 2005, ApJ, 635, L37
Rojas-Ayala, B., Covey, K. R., Muirhead, P. S., & Lloyd, J. P. 2010, ApJ, 720, L113
Schlegel, D. J., Finkbeiner, D. P., & Davis, M. 1998, ApJ, 500, 525
Ségransan, D., Kervella, P., Forveille, T., & Queloz, D. 2003, A&A, 397, L5
Shkolnik, E. L., Hebb, L., Liu, M. C., Reid, I. N., & Collier Cameron, A. 2010, ApJ, 716, 1522
Slesnick, C. L., Carpenter, J. M., & Hillenbrand, L. A. 2006, AJ, 131, 3016
Soderblom, D. R. & Mayor, M. 1993, AJ, 105, 226
Southworth, J. 2008, MNRAS, 386, 1644
Southworth, J., Bruntt, H., & Buzasi, D. L. 2007a, A&A, 467, 1215
Southworth, J., Bruntt, H., & Buzasi, D. L. 2007b, A&A, 467, 1215
Southworth, J. & Clausen, J. V. 2007, A&A, 461, 1077
Southworth, J., Maxted, P. F. L., & Smalley, B. 2004a, MNRAS, 349, 547
Southworth, J., Maxted, P. F. L., & Smalley, B. 2004b, MNRAS, 351, 1277
Southworth, J., Maxted, P. F. L., & Smalley, B. 2005a, A&A, 429, 645
Southworth, J., Smalley, B., Maxted, P. F. L., Claret, A., & Etzel, P. B. 2005b, MNRAS, 363, 529
Southworth, J., Zucker, S., Maxted, P. F. L., & Smalley, B. 2004c, MNRAS, 355, 986
Stassun, K. G., Mathieu, R. D., & Valenti, J. A. 2007, ApJ, 664, 1154
Torres, G., Andersen, J., & Giménez, A. 2010, A&A Rev., 18, 67
Torres, G., Lacy, C. H., Marschall, L. A., Sheets, H. A., & Mader, J. A. 2006, ApJ, 640, 1018
Torres, G. & Ribas, I. 2002, ApJ, 567, 1140
Vaccaro, T. R., Rudkin, M., Kawka, A., et al. 2007, ApJ, 661, 1112
van Hamme, W. 1993, AJ, 106, 2096
Viti, S., Jones, H. R. A., Maxted, P., & Tennyson, J. 2002, MNRAS, 329, 290
Viti, S., Jones, H. R. A., Schweitzer, A., et al. 1997, MNRAS, 291, 780
West, A. A., Morgan, D. P., Bochanski, J. J., et al. 2011, AJ, 141, 97
Woolf, V. M., Lépine, S., & Wallerstein, G. 2009, PASP, 121, 117

Woolf, V. M. & Wallerstein, G. 2006, PASP, 118, 218
Zahn, J. 1977, A&A, 57, 383
Zahn, J.-P. 1975, A&A, 41, 329
Zucker, S. & Mazeh, T. 1994, ApJ, 420, 806